

Annual Review of Fluid Mechanics
Coalescence Dynamics

Jens Eggers,¹ James E. Sprittles,²
and Jacco H. Snoeijer³

¹School of Mathematics, University of Bristol, Bristol, United Kingdom

²Mathematics Institute, University of Warwick, Coventry, United Kingdom

³Physics of Fluids Group, Faculty of Science and Technology, University of Twente, Enschede, The Netherlands; email: j.h.snoeijer@utwente.nl

ANNUAL
REVIEWS **CONNECT**

www.annualreviews.org

- Download figures
- Navigate cited references
- Keyword search
- Explore related articles
- Share via email or social media

Annu. Rev. Fluid Mech. 2025. 57:61–87

First published as a Review in Advance on
July 26, 2024

The *Annual Review of Fluid Mechanics* is online at
fluid.annualreviews.org

<https://doi.org/10.1146/annurev-fluid-121021-044919>

Copyright © 2025 by the author(s). This work is licensed under a Creative Commons Attribution 4.0 International License, which permits unrestricted use, distribution, and reproduction in any medium, provided the original author and source are credited. See credit lines of images or other third-party material in this article for license information.



Keywords

droplets, bubbles, coalescence, capillarity, singularities, complex fluids

Abstract

The merging of two fluid drops is one of the fundamental topological transitions occurring in free surface flow. Its description has many applications, for example, in the chemical industry (emulsions, sprays, etc.), in natural flows driving our climate, and for the sintering of materials. After the reconnection of two drops, strongly localized surface tension forces drive a singular flow, characterized by a connecting liquid bridge that grows according to scaling laws. We review theory, experiment, and simulation of the coalescence of two spherical drops for different parameters and in the presence of an outer fluid. We then generalize to other geometries, such as drops spreading on a substrate and in Hele–Shaw flow, and we discuss other types of mass transport, apart from viscous flow. Our focus is on times immediately after reconnection and on the limit of initially undeformed drops at rest relative to one another.

1. INTRODUCTION AND HISTORICAL PERSPECTIVE

The coalescence of liquid drops, or other volumes of liquid, is the other fundamental process, complementary to breakup, that takes place in free surface flow (Eggers 1997, Tryggvason et al. 2011, Popinet 2018, Anthony et al. 2023). It is near such singularities where new structures, such as drops, are born and where rapid motion takes place, which imprints its characteristics on the dynamics. The neighborhood of the places of topological transitions is therefore of special physical and technological interest and is often characterized by a simplifying self-similar structure. This makes the transitions amenable to analytical mathematical treatment, which is unusual for highly complex and nonlinear free surface flows. Clearly, coalescence processes are of fundamental importance in industrial applications (Kamp et al. 2017), for example, in the physics of emulsions (Chesters 1991), for oil recovery (Kavehpour 2015), for inkjet printing (Lohse 2022), for the collision rates in flows containing fluid particles (Liao & Lucas 2010), and for the sintering process (Rahaman 2010), in which a uniform material is created through the merging of individual particles. Models for coalescence have also been applied in biology, rationalizing the merging of cell nucleoli as well as clumps of cells (Pokluda et al. 1997, Flenner et al. 2012, Caragine et al. 2018, Grosser et al. 2021).

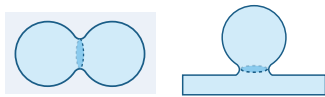
Curiously, the driver in both breakup and coalescence is surface tension. In breakup, a sufficiently extended fluid column releases surface energy by reducing its radial extent, which then goes to zero in finite time (Eggers & Villermaux 2008, Eggers & Fontelos 2015, Anthony et al. 2023), but merging of spheres also leads to a reduction of surface area. Once two drops are reconnected by a very small liquid bridge, surface tension will thus induce a very rapid coalescence motion.

The breakup process involves vanishing length scales and timescales, well separated from those describing smooth motion, leading to universal scaling exponents and self-similar surface profiles, independent of initial conditions and even fluid parameters; thus in breakup the geometry is generated self-consistently and the singularity is encountered during the final stages of breakup. By contrast, in coalescence the motion starts in the singular regime and the geometry is imposed by the initial condition. **Figure 1** provides an overview of typical coalescence geometries: In contrast to breakup, the resulting coalescence dynamics is not universal, but strongly depends on the imposed geometry, e.g., by confinement of the drops (Ryu et al. 2023). Additional complexity comes from the fact that the outer (dispersed) phase also plays a major role in coalescence, even if its viscosity is very small. The reason is that the outer fluid is confined to a very small gap between the two drops, and lubrication effects come into play.

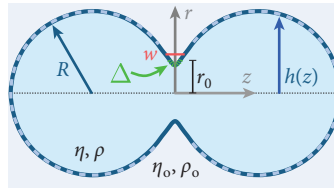
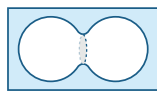
Coalescence has until recently been considered on a large-scale and qualitative level only (Kamp et al. 2017), the earliest work being directed toward the conditions under which coalescence takes place in the first instance (for example, Reynolds 1900). Charles & Mason (1960b) and Thoroddsen & Takehara (2000) have produced photographic sequences of the coalescence of a drop with a bath, which leads to a cascade of coalescence events. The earliest systematic efforts to understand the dynamics of coalescence quantitatively, from experimental (Kuczynski 1949), theoretical (Frenkel 1945, Kuczynski 1949, Hopper 1991), and numerical (Nichols & Mullins 1965) perspectives, are related to the (viscous) sintering problem. Other surface tension-driven transport mechanisms, which dominate at temperatures at which the drops are solid, have also been considered widely (Rahaman 2010). The reason for the relative neglect of the initial coalescence process is the tremendous speed of its motion, which makes experimental (Thoroddsen et al. 2008) and numerical (Sprittles & Shikhmurzaev 2014b, Anthony et al. 2023) approaches very demanding (see the sidebar titled Numerical Methods). The very small width of the gap between two spherical drops, in addition, obscures imaging of the liquid bridge and requires very high numerical resolution.

Spherical or cylindrical (two-dimensional) coalescence

a Drops, drop and bath



b Bubbles

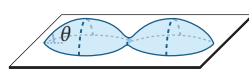


Geometrically similar coalescence

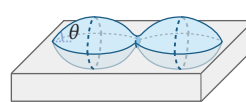
c Conical drops



d Drops on a substrate

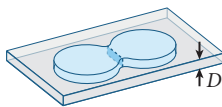


e Liquid lenses

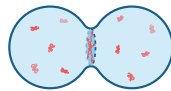


Other geometries or transport mechanisms

f Hele–Shaw



g Viscoelastic coalescence



h Diffusive coalescence

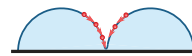


Figure 1

The dynamics of coalescence is highly dependent on the geometry of the drops at the moment of contact. Spherical/cylindrical coalescence involves (a) two drops or a drop merging with a bath or (b) bubbles that are spherical/cylindrical upon the moment of contact. The geometry imposes a hierarchy of scales: drop radius R , bridge radius r_0 , bridge width $w = r_0^2/R$, and meniscus curvature $\Delta = r_0^3/R^2$. The droplet viscosity and density are denoted η and ρ , respectively, while η_0 and ρ_0 refer to the viscosity and density of the surrounding outer fluid. Geometrically similar coalescence refers to geometrically similar initial conditions, where different directions are related by an angle. Examples are (c) conical drops, (d) drops on a substrate, and (e) liquid lenses. The review further covers other geometries and non-Newtonian transport mechanisms, such as (f) drops in a Hele–Shaw cell, (g) viscoelastic drops, where the schematic illustrates the stretching of polymers inside the bridge, and (h) coalescence by diffusive transport. Figure adapted from illustrations by Alexandros Oratis.

A complete picture of coalescence would require a full understanding of all stages of the process that leads to the complete merging of drops:

1. Approach. Two drops first need to be brought together, which in general will be at a finite velocity and impact parameter. For example, in a head-on collision of two spherical drops of radius R traveling at relative speed U , the hypothetical geometrical overlap between the two spheres yields a bridge radius of $r_0 = \sqrt{URt}$, which competes with the singular motion engendered by surface tension and indicates a nonuniversal dependence of coalescence dynamics on the impact speed. At small distances, draining of the thin film between the two drops will become important (Charles & Mason 1960a, Davis et al. 1989, Chan et al. 2011, Kamp et al. 2017). As a result, drops will in general be deformed by lubrication forces, in which rarefied gas effects become crucial (Li 2016, Sprittles 2024).

NUMERICAL METHODS

Until relatively recently, numerical methods have been unable to confirm many of the theoretical predictions for coalescence. This is because they either (a) have captured the global shape of the droplets, without resolving small scales of bridge growth (i.e., neglecting $r_0/R \ll 1$), or (b) have focused, or zoomed in, on the early growth, often in specific flow regimes, without being able to simulate the entire drop's motion (i.e., considering only $r_0/R \ll 1$).

For (a), numerical simulations are able to reproduce coalescing drop shapes and can often recover inviscid (Menchaca-Rocha et al. 2001, Baroudi et al. 2014) and viscous (Baroudi et al. 2016) scalings—these are usually based on interface capturing schemes (marker and cell, volume of fluid, lattice Boltzmann, etc.). For (b), boundary integral methods have been deployed to compute both inviscid and viscous limits near the bridge front. Here, in the inviscid case, the absence of an outer fluid causes the free surface to overturn and entrap toroidal bubbles (Oguz & Prosperetti 1989, Duchemin et al. 2003). However, while some experimental evidence for entrapment has been given (Aryafar & Kavehpour 2008, Fezzaa & Wang 2008), simulations suggest that tiny amounts of outer fluid can prevent the formation of bubbles (Sprittles & Shikhmurzaev 2014b) and lead instead to the formation of pockets of gas (also often referred to as bubbles) in front of the evolving neck, as also seen in the viscous case (Eggers et al. 1999).

Considering first a drop in a vacuum, in the viscous regime the smallest length scale is the bridge's radius of curvature $\sim r_0^3/R^2$. Then, for a millimeter-sized drop, when $r_0 \approx 1 \mu\text{m}$ the ratio of the minimum length scale to drop size $\sim (r_0/R)^3$ is $\approx 10^{-9}$. Then, for example, to capture this scale with 10 volume-of-fluid cells one needs to reach level 30 (as $1/2^{30} \approx 10^{-10}$), well beyond current capabilities. Consequently, most of the simulations probing the earliest stages of coalescence have been performed by interface tracking methods, specifically arbitrary Lagrangian–Eulerian finite-element method (ALE-FEM) codes, which can be tailored to resolve singular dynamics [see the review by Anthony et al. (2023)].

For ALE-FEM, one has to initiate the simulation with initial conditions on the velocity profile with a drop shape that creates a finite-sized bridge $r_{0,IC}$. The work with ALE-FEM codes began in a series of articles (Sprittles & Shikhmurzaev 2012, 2014a,b) initially focused on forming interfaces, where the effect of the outer fluid is also accounted for. More recently Anthony et al. (2020) reached even smaller scales in the single-fluid problem. To test both theories proposed in the literature, as well as to compare to experiments, typically one needs $r_{0,IC}/R = 10^{-4}$ to give a few decades of reliable comparison (to satisfy $r_0 > 10r_{0,IC}$ and $r_0/R \ll 1$). For a drop in gas, the smallest scale is at most the bridge width, alleviating somewhat the requirements on the grid—for the example above we would now only need level 23! Sprittles & Shikhmurzaev (2014b) and Anthony et al. (2020) established that the initial conditions used in the computation can have a profound influence on the scalings observed, with either underresolved computation or an offset in the initial conditions potentially leading to different (incorrect) scalings.

2. Reconnection. Microscopic interactions, through long-ranged intermolecular forces or charge effects, lead to a joining of the two interfaces. This can lead to a jump to contact, i.e., reconnection before the equilibrium shapes of the drops overlap (Quinn et al. 2013; Chireux et al. 2018; Beaty & Lister 2022, 2023; Deblais et al. 2024); the effect of thermal noise may also play a role (Perumanath et al. 2019).
3. Coalescence. This is the initial surface tension–driven merging of two fluid volumes, which is the focus of this review. During this phase the dynamics is confined to the rapid motion of a small liquid bridge connecting the two drops, the size of which is small compared to the drops. As we shall see, in these earliest stages the centers of mass of the drops move little, since the amount of fluid set in motion by the moving meniscus is small. On account of the locality of the motion, the dynamics is characterized by scaling laws, but with significant exceptions: There can be logarithmic corrections, and profiles do not necessarily exhibit self-similar shapes.

4. Merging. During the actual merging of the drops, the bulk of the original drops interpenetrates to form a larger drop (Ashgriz & Poo 1990, Verdier 2001); this is the stage in which most of the mass transfer takes place, and the subsequent dynamics can be quite complicated (Planchette et al. 2012).

This review is dedicated to the coalescence regime that describes the early dynamics after two drops have been joined at a point. Experimentally and numerically, this requires a careful preparation of the initial conditions and very high spatial and temporal resolution. We focus on Newtonian flow of liquid drops and bubbles for the geometries indicated in **Figure 1a–f**; we also discuss other transport mechanisms that are relevant, e.g., for sintering, as sketched in **Figure 1g,b**. We begin with a discussion of the timescales and length scales of Newtonian drop coalescence.

Drops of honey merge very slowly, the surface energy driving the motion being eaten up by viscous friction, while, during the rapid coalescence dynamics of water drops, surface tension is opposed only by inertia, the drops being nearly perfectly inviscid. Using the relevant material parameters for Newtonian drops (surface tension γ , dynamic viscosity η , density ρ), a unique intrinsic length scale ℓ_v and a timescale t_v can be constructed (Peregrine et al. 1990, Eggers 1993), at which surface tension, viscosity, and inertia are balanced. The size of ℓ_v relative to the characteristic lengths of the problem determines which regime, viscous or inertial, one is in.

For water, one obtains $\ell_v \approx 14$ nm, while for liquid honey ℓ_v reaches up to several meters. This large variability in ℓ_v explains why such vastly different dynamics can be observed for millimeter-sized drops. Indeed, introducing the drop size R as an extrinsic length scale, the dimensionless ratio $\ell_v/R \equiv \text{Oh}^2$ involves the Ohnesorge number, which quantifies the relative importance of viscosity to inertia on the global scale of the drop. The Ohnesorge number can also be written as a ratio of timescales $\text{Oh} = \tau_v/\tau_i$, using the viscous time τ_v and inertial time τ_i . These represent the typical times for the complete merging of two drops in the viscous and inertial regimes, respectively.

In this review we concentrate on the initial stages of coalescence, for which the minimum bridge radius of the fluid neck connecting the two drops $r_0(t) \ll R$ (see **Figure 1**). In such an asymptotic limit, and barring logarithmic corrections, one expects the dynamics to have power-law form (Eggers & Fontelos 2015), so the asymptotic regimes for the viscous and inertial bridge dynamics are described, respectively in the viscous and inertial limits, by

$$\frac{r_0}{R} \sim \left(\frac{t}{\tau_v}\right)^\alpha, \quad \frac{r_0}{R} \sim \left(\frac{t}{\tau_i}\right)^\beta. \quad 1.$$

The exponents α and β are not universal but depend on the coalescence geometry, as we will review in detail (cf. **Tables 1** and **2**). Special attention will be given to the crossover between viscous and inertial coalescence.

2. SCALING LAWS: INFLUENCE OF DROP GEOMETRY

2.1. Local Versus Global Energy Balance

The coalescence of drops is driven by the tendency to reduce surface energy: Two drops have a greater surface area than a single merged drop. Refining this argument, Frenkel (1945) put forward the influential idea, both in engineering (Pokluda et al. 1997, Rahaman 2010) and in biology (Flenner et al. 2012, Caragine et al. 2018, Grosser et al. 2021), that the rate of coalescence is determined by a balance of the local rate of energy \dot{E}_v freed, with the viscous dissipation inside the drop. The dissipative power can be estimated by $P_\eta \sim \eta \dot{\epsilon}^2 \mathcal{V}$, where $\dot{\epsilon}$ is the typical rate of deformation and \mathcal{V} the characteristic volume that is sheared.

Focusing on the early stages of coalescence, Frenkel (1945) balances $\dot{E}_v = \frac{d}{dt}(\pi\gamma r_0^2)$ with dissipation taking place over the entire drop, i.e., $\mathcal{V} \sim R^3$. This gives the incorrect prediction

$\ell_v = \eta^2/(\gamma\rho)$:
intrinsic length scale

$t_v = \eta^3/(\gamma^2\rho)$:
intrinsic timescale

$\text{Oh} = \eta/\sqrt{\rho R\gamma}$:
Ohnesorge number,
which measures the
relative importance of
viscous to inertial
effects

$\tau_v = \eta R/\gamma$: viscous
timescale based on the
size of the drop

$\tau_i = \sqrt{\rho R^3/\gamma}$: inertial
timescale based on the
size of the drop

Table 1 Scaling laws in the viscous regime: $\dot{E}_\gamma = P_\eta$

	Capillary power $\frac{d}{dt}(\gamma\mathcal{A})$	Viscous dissipation $\eta\dot{\epsilon}^2\mathcal{V}$	Bridge scaling $r_0(t)$	Exponent α	Section(s)
Spherical drops	$\frac{d}{dt}(\gamma r_0^2)$	$\eta\left(\frac{\dot{r}_0}{r_0}\right)^2 r_0^3$	$\frac{\gamma t}{\eta} \ln(R/r)$	1 (log corr.)	Sections 2.2 and 3.1
Spherical bubbles	$\frac{d}{dt}(\gamma r_0^2)$	$\eta\left(\frac{\dot{r}_0}{r_0}\right)^2 r_0^2 w$	$\left(\frac{t}{\tau_v}\right)^{1/2} R$	1/2	Sections 2.2 and 3.3
Hele-Shaw ($D \ll r_0$)	$\frac{d}{dt}(\gamma D r_0)$	$\eta\left(\frac{\dot{r}_0}{D}\right)^2 r_0 D w$	$\left(\frac{t}{\tau_v}\right)^{1/4} \sqrt{RD}$	1/4	Section 2.4
Sessile drops (side view, two-dimensional)	$\frac{d}{dt}(\gamma\mathcal{L})$	$\eta\dot{\epsilon}^2\mathcal{A}$	$b_0(t)$	α	
Substrate ($\theta \ll 1$)	$\frac{d}{dt}(\gamma b_0\theta)$	$\eta\left(\frac{\dot{b}_0/\theta}{b_0}\right)^2 \frac{b_0^2}{\theta}$	$\frac{\gamma t}{\eta} \theta^4$	1	Sections 2.3 and 4.1
Liquid pool ($\theta \ll 1$)	$\frac{d}{dt}(\gamma b_0\theta)$	$\eta\left(\frac{\dot{b}_0}{b_0}\right)^2 \frac{b_0^2}{\theta}$	$\frac{\gamma t}{\eta} \theta^2$	1	Sections 2.3 and 4.1

Cases for which the drop curvature matters invoke $w = r_0^2/R$ as the bridge width and $\tau_v = \eta R/\gamma$ as the viscous timescale.

$r_0 \sim \sqrt{\gamma R t/\eta}$ for spherical drops: In reality the initial motion and thus dissipation are concentrated in a small neck region, with the coalescing drops remaining static.

Yet in the spirit of Frenkel's calculation, we use energy balance as a unifying approach to understand the initial coalescence dynamics in a broad class of coalescence geometries (**Figure 1**), by choosing an appropriate local form of the control volume \mathcal{V} . In the viscous regime, all the capillary power (surface energy $\gamma\mathcal{A}$ released per unit time; $\gamma\mathcal{L}$ for a two-dimensional object) is dissipated instantaneously by the viscous flow inside the bridge, with $\dot{\epsilon}^2$ and \mathcal{V} to be identified. In the inertial regime, viscous dissipation is subdominant and all the released capillary energy is assumed to be converted into kinetic energy of the moving fluid. Therefore, it is natural to invoke the energy balance $E_\gamma = E_{\text{kin}} \sim \rho v^2 \mathcal{V}$ (rather than a power balance), where v is the typical velocity inside the bridge. Different coalescence geometries lead to different expressions for E_γ , E_{kin} , and P_η , and the

Table 2 Scaling laws in the inertial regime: $E_\gamma = E_{\text{kin}}$

	Capillary energy $\gamma\Delta\mathcal{A}$	Kinetic energy $\rho v^2\mathcal{V}$	Bridge scaling $r_0(t)$	Exponent β	Section(s)
Spherical drops	γr_0^2	$\rho \dot{r}_0^2 r_0^2 w$	$\left(\frac{t}{\tau_i}\right)^{1/2} R$	1/2	Sections 2.2 and 3.2
Spherical bubbles	γr_0^2	$\rho \dot{r}_0^2 r_0^2 w$	$\left(\frac{t}{\tau_i}\right)^{1/2} R$	1/2	Sections 2.2 and 3.3
Conical drops	γr_0^2	$\rho \dot{r}_0^2 r_0^3$	$\left(\frac{\gamma t^2}{\rho}\right)^{1/3}$	2/3	Section 2.3
Sessile drops (side view, two-dimensional)	$\gamma\Delta\mathcal{L}$	$\rho v^2\mathcal{A}$	$b_0(t)$	β	
Substrate ($\theta < 90^\circ$)	γb_0	$\rho \dot{b}_0^2 b_0^2$	$\left(\frac{\gamma t^2}{\rho}\right)^{1/3}$	2/3	Sections 2.3 and 4.2
Substrate ($\theta = 90^\circ$)	γb_0	$\rho \dot{b}_0^2 b_0 w$	$\left(\frac{t}{\tau_i}\right)^{1/2} R$	1/2	Section 4.2
Liquid pool ($\theta \ll 1$)	$\gamma b_0\theta$	$\rho\left(\frac{\dot{b}_0}{\theta}\right)^2 \frac{b_0^2}{\theta}$	$\left(\frac{\gamma t^2 \theta^4}{\rho}\right)^{1/3}$	2/3	Sections 2.3 and 4.2

Cases for which the drop curvature matters invoke $w = r_0^2/R$ as the bridge width and $\tau_i = \sqrt{\rho R^3/\gamma}$ as the inertial timescale.

resulting bridge dynamics $r_0(t)$ is not at all universal—as discussed in detail below (cf. **Tables 1** and **2**).

2.2. Spheres

We start by discussing the coalescence of spherical drops and bubbles. While we focus on the case where the spheres have identical radii R , our scaling arguments are equally valid when drop sizes are different or for a drop merging with a bath (**Figure 1a**).

2.2.1. Drops. Assuming a bridge radius r_0 , the characteristic width w of the bridge is much smaller and scales as $w = r_0^2/R$ (**Figure 1a**), where in the case of unequally sized drops R would be an effective radius. For a typical millimeter-sized drop, a bridge radius of a micrometer implies the width to be as small as a nanometer. From the energetic point of view, the width of the bridge can be neglected when computing the released capillary energy, $E_\gamma \sim \gamma r_0^2$. The kinetic energy can be estimated using the velocity $v \sim \dot{r}_0$, which is reached inside the bridge over a volume $\mathcal{V} \sim r_0^2 w \sim r_0^4/R$. The balance of surface and kinetic energies $E_\gamma = \rho v^2 \mathcal{V}$ then gives the inertial scaling $r_0 \sim (\gamma R/\rho)^{1/4} t^{1/2}$. The viscous scaling is more subtle. The dissipated power can be estimated using the rate of deformation $\dot{\epsilon} \sim \dot{r}_0/r_0$. However, owing to the nonlocal nature of viscous flow, the region over which dissipation occurs extends in all directions but is cut off at the scale of the two opposing menisci to give $\mathcal{V} \sim r_0^3$. The balance $\dot{E}_\gamma = \eta \dot{\epsilon}^2 \mathcal{V}$ then gives $r_0 \sim \eta t/\gamma$. This scaling argument does not capture logarithmic corrections of the actual viscous coalescence dynamics, which goes like $r_0 \sim t \ln t$. Such corrections call for a more detailed approach beyond the simplified scaling analysis (see Section 3.1). We note there is an equivalence of coalescence in two and three dimensions, in the sense that cylinders and spheres exhibit the same scaling laws. This is because the width of the gap is much smaller than r_0 , so the meniscus of coalescing spheres is almost straight on the scale of w and thus corresponds to the straight menisci of coalescing cylinders.

2.2.2. Experiments. The first experiments to study the asymptotics of drop coalescence found reasonable agreement with the expected scaling in the low-viscosity (Menchaca-Rocha et al. 2001, Wu et al. 2004, Aarts et al. 2005) and high-viscosity (Yao et al. 2005) limits. Even if the temporal resolution is high, the main obstacle is the ability to look into the gap of width w between the drops. As a result, the optical method is typically limited to measuring w down to a few micrometers, which typically involves r_0 down to 50 μm and thus $r_0/R \gtrsim 0.05$, making it difficult to access the asymptotic behavior as $r_0 \rightarrow 0$.

To improve on this, an electrical method was developed (Case & Nagel 2008, Paulsen 2013), which relies on measuring the impedance of the entire coalescence cell, comparing it to an electrostatic calculation based on two hemispheres joined by a neck of radius r_0 . The resulting values of r_0 were found to be insensitive to the modeling of the neck and agreed very well with optical measurements in the region of overlap. The electrical method allows for tracking r_0 down to timescales of 100 ns, so that r_0 is measured down to a radius of 1 μm , an improvement of two orders of magnitude.

Following Paulsen et al. (2011), Paulsen (2013), and Xia et al. (2019), in **Figure 2** experimental data have been rescaled using the crossover radius $r_c = ROh$ and crossover time $t_c = \tau_v Oh$, which provides a useful collapse of experimental data over a wide range of Oh . The experiments agree with numerical data obtained from solving the Navier–Stokes equations, including the effect of the surrounding air (computed for $Oh = 0.01$ and 1). As is discussed in more detail in Section 3.1, these numerical data confirm the presence of logarithmic corrections in the viscous regime and fall within the experimental scatter, which is up to a factor of 3. Finally, the profiles observed in numerical simulations are in excellent agreement with those obtained experimentally

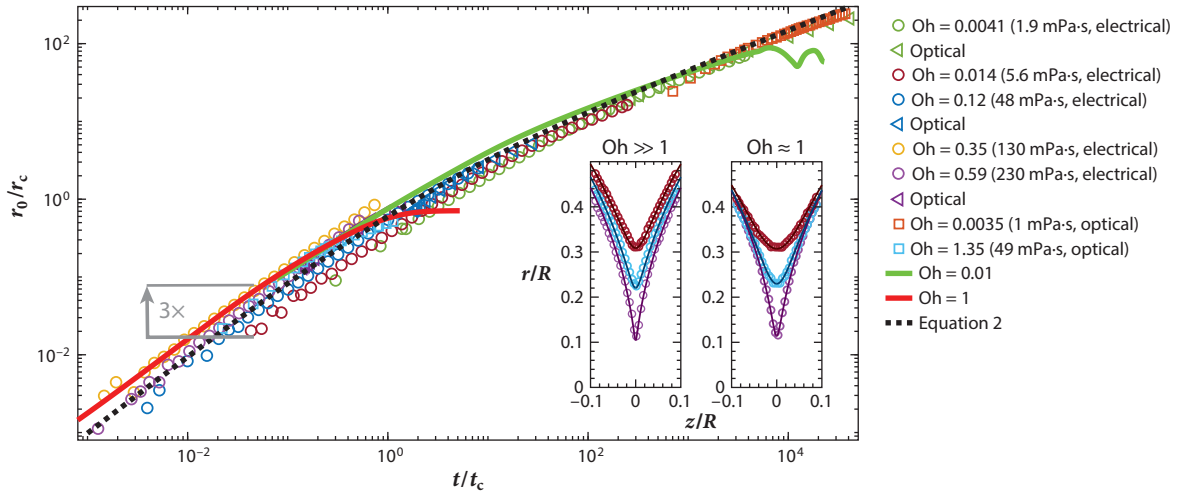


Figure 2

Scaling plot of available data for spherical drop coalescence, comparing experimental data (*symbols*) and numerical calculations replotted from Sprittles & Shikhmurzaev (2014b) (*solid lines*), taking $\eta_{\text{air}} = 0.018 \text{ mPa}\cdot\text{s}$ (corresponding to $\lambda = 2.2 \times 10^4 \text{ Oh}$ for the water–glycerol mixtures considered here). Data are scaled using the crossover scales $r_c = R\text{Oh}$ and $t_c = \tau_v \text{Oh}$, which dictate the crossover from viscous ($t \ll t_c$) to inertial dynamics ($t \gg t_c$). All experimental data are for water–glycerol drops in the presence of air. Circles/triangle are from Paulsen (2013) for electrical/optical and squares are from Thoroddsen et al. (2005b). These datasets were chosen as they use electrical triggers to define accurately the initial contact time. Data from Paulsen (2013) were chosen either as optical and electrical data were available or to fill in empty regions of the plot. The dashed line represents the empirical crossover function (Equation 2) that interpolates between the viscous and inertial regimes. The spread in the experimental data for r_0 is up to a factor of 3. (*Inset*) Experimentally recorded neck shapes (*symbols*) for two different viscosities in air at $\text{Oh} = 370$ and $\text{Oh} = 0.62$ from Paulsen (2013), compared to numerical simulations at $\text{Oh} = \infty$ (Stokes) and $\text{Oh} = 1$, respectively. The numerical profiles from Sprittles & Shikhmurzaev (2014b) have been selected for the minimum radius to match at the earliest instance.

in the optically accessible range (**Figure 2**, inset). We thus conclude that simulations, accounting for the influence of the outer air, give a consistent description of the available experimental data.

2.2.3. Crossover. Dimensional analysis shows that the minimum bridge radius can be written in the form $r_0 = R\hat{f}(t/\tau_v, \text{Oh}, \lambda)$, where $\lambda = \eta/\eta_o$ is the viscosity ratio; a small outer density (i.e., density ratio $\rho/\rho_o \gg 1$) is found to have a vanishing effect on the dynamics. However, we see in Section 3.3 that even a small outer viscosity (large λ) changes the structure of the narrow gap between the spheres significantly. **Figure 2** shows that the dependence on the remaining parameters τ_v and Oh can be collapsed in a crossover function of a single variable (Paulsen et al. 2011),

$$\frac{r_0}{r_c} = f(\xi) = \left[\frac{1}{C_v \xi} + \frac{1}{C_i \sqrt{\xi}} \right]^{-1}, \quad \text{with } \xi = t/t_c, \quad 2.$$

that interpolates between the viscous scaling $r_0/R = C_v t/\tau_v$ and the inertial scaling $r_0/R = C_i \sqrt{t/\tau_v}$. In the plot we used the empirical values $C_v = 1$ and $C_i = 1.5$. Even though the rescaling of data is very good, we emphasize that the collapse in **Figure 2** must be considered approximate: A universal crossover function does not exist even for $\lambda = \infty$, owing to logarithmic corrections to the viscous regime (see Section 3.1).

2.2.4. Bubbles. The geometry of bubble coalescence superficially resembles that of spherical drops, but the liquid is now confined to a thin sheet on the exterior of the spheres. This sheet is the only portion of the liquid to be set in motion, as the liquid film retracts under the influence

$\lambda = \eta/\eta_o$: viscosity ratio relative to outer atmosphere

ρ/ρ_o : density ratio, neglected throughout for droplet coalescence

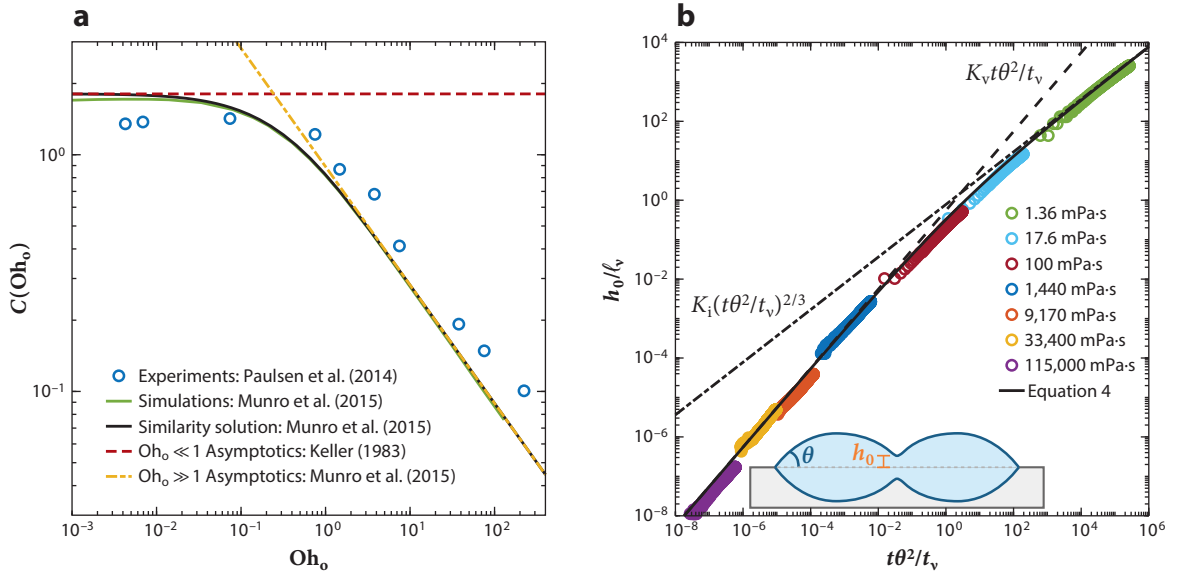


Figure 3

Two examples of viscous to inertial crossover. (a) For spherical bubbles, the bridge dynamics follows $r_0 \sim t^{1/2}$ in both the viscous and inertial regimes. The crossover shows up in the prefactor $C(\text{Oh}_o)$ as defined by Equation 3, which is plotted as a function of Oh_o . Experimental measurements (symbols) (Paulsen et al. 2014), numerical simulations (green line), similarity solutions (black line), a viscous asymptote (yellow dashed line) (Munro et al. 2015), and an inertial asymptote (red dashed line) (Keller 1983) are shown. (b) Liquid lenses present a case of geometrically similar coalescence: The side view bridge height h_0 crosses over as time evolves, from $h_0 \sim t$ (viscous) to $h_0 \sim t^{2/3}$ (inertial). Experiments (symbols), a crossover function (Equation 4; solid line), a viscous asymptote (dash-dotted line; $K_v = 0.552$), and an inertial asymptote (dashed line; $K_i = 0.781$) (Hack et al. 2020) are shown.

of surface tension; the Ohnesorge number Oh_o below now refers to the viscosity η_o of the outer fluid alone. Perhaps surprisingly, the bridge radius now scales as $r_0 \sim t^{1/2}$ for both the viscous and inertial regimes (Paulsen et al. 2014, Munro et al. 2015). The resulting dynamics can therefore be captured by the form

$$\frac{r}{R} = C(\text{Oh}_o) \left(\frac{t}{\tau_i} \right)^{1/2}, \quad 3.$$

where $C(\text{Oh}_o)$ is a dimensionless prefactor that accounts for the slowing down upon increasing viscosity. Experimental data (Paulsen et al. 2014) for the prefactor are plotted in **Figure 3a**, together with model predictions obtained from direct simulations and from a similarity analysis based on a thin film approximation (Munro et al. 2015).

The retraction of the film separating the bubbles comes with a release of capillary energy $E_\gamma \sim \gamma r_0^2$. At low viscosity, this retraction results in the sheet fluid of volume $\sim r_0^2 w \sim r_0^4/R$ being collected into a growing annular rim of volume $\mathcal{V} \sim r_0^4/R$. The scaling laws for both E_γ and E_{kin} therefore turn out identical to that of drop coalescence, and the same scaling $r_0 \sim t^{1/2}$ ensues in the inertial regime. In the specific case of $\text{Oh}_o = 0$, the original arguments of Taylor (1959) and Culick (1960) can be turned into an exact result, invoking momentum conservation (Keller 1983). During coalescence, the fluid up to a certain radius r_0 is collected inside a rim, which from the shape $z = r^2/(2R)$ of the unperturbed sheet gives a volume $\mathcal{V}_{\text{rim}} = \pi r_0^4/(2R)$. Since the force on the rim exerted by the surface tension per unit length is 2γ , Newton's equation now reads $4\pi\gamma r_0 = d(\mathcal{V}_{\text{rim}}\dot{r}_0)/dt$, the solution of which yields Equation 3 with $C = (32/3)^{1/4} \approx 1.81$. The

Geometrically similar coalescence: coalescence with geometrically similar initial conditions exhibits bridge growth that is independent of global drop size; it involves $r_0 \sim t$ (viscous flow) and $r_0 \sim t^{2/3}$ (inertial flow)

same numerical value was found solving similarity equations based on this thin sheet approximation (Munro et al. 2015). The experimental value for the prefactor is slightly lower: $C \approx 1.4$ (Paulsen et al. 2014). The mismatch has been attributed to the (optical) experiment not being able to access the asymptotic regime (Anthony et al. 2017); this is consistent with the absence of a visible rim in experiments (Oratis et al. 2023).

In the viscous regime, bubble coalescence is very different from drop coalescence, since now the flow is confined to the liquid film between the spheres. The relevant volume in which dissipation occurs is $\mathcal{V} \sim r_0^4/R$ (rather than r_0^3 for drops), yielding bridge dynamics $r_0 \sim t^{1/2}$ (rather than $t \ln t$ for drops). Similarity analysis for the full range of Oh_o is possible, which in the viscous regime reduces to $C = 0.8909/\sqrt{\text{Oh}_o}$ (Munro et al. 2015), in line with the experimental trend.

2.3. Geometrically Similar Initial Conditions

Coalescence exponents are not universal but depend on the fluid geometry upon contact. However, some degree of universality is recovered in the special case of geometrically similar initial conditions. This refers to geometries that are invariant under an isotropic rescaling of all spatial coordinates. Prototypical examples are wedges (Miksis & Vanden-Broeck 1999, Keller et al. 2000, Billingham & King 2005) and cones (Bartlett et al. 2015), for which scales in orthogonal directions are related by an angle. For geometrically similar coalescence, the only relevant scale is the local size of the bridge, and the global drop size R plays no role during the initial stages. Inspecting Equation 1, we see the independence of R implies an exponent $\alpha = 1$ for viscous coalescence and $\beta = 2/3$ for inertial dynamics. Below, we report experiments that fall into this class of geometrically similar coalescence.

2.3.1. Spherical drops with conical tips. Charged drops in a strong electric field can lose their rounded shapes and develop conical tips, similar to Taylor cones (de la Mora 2007). When two charged drops are in close vicinity, the geometry prior to coalescence is thus not necessarily given by a rounded interface but can consist of cones with a well-defined cone angle θ (Figure 1c). An interesting feature is that conical drops only merge for angles above a critical value θ_c (Bird et al. 2009). For smaller cone angles, a connecting bridge would actually pinch rather than merge. Assuming inviscid dynamics, the critical angle $\theta_c = 65.3^\circ$ was determined from similarity solutions (Bartlett et al. 2015), consistent with experiment.

Once coalescence occurs in the inertial regime, the minimum bridge radius evolves according to $r_0 \sim (\gamma/\rho)^{1/3} t^{2/3}$, independently of the global size of the drop R (Bird et al. 2009). The independence of the drop size is due to the geometrically similar conical shape: The height and the width of the bridge are both proportional to r_0 , the two scales being related by the cone angle. The exponent $2/3$ follows on dimensional grounds. Likewise, if viscosity is dominant, dimensional analysis without invoking R yields $r \sim \gamma t/\eta$.

2.3.2. Sessile drops. In many circumstances drops are in contact with a substrate (condensation, rain on a windshield, spraying, printing, etc.), giving rise to slowly spreading or stationary sessile drops. The geometry of such drops consists of a spherical cap [or a puddle, in case gravity is important (de Gennes et al. 2004)], which makes a well-defined contact angle θ with the substrate (see Figure 1d). Another case of sessile drops is droplets that are floating on a liquid pool (see Figure 1e) (de Gennes et al. 2004, Burton & Taborek 2007). A prototypical example of these so-called liquid lenses is the fatty drops floating in a bowl of soup. The geometry of a liquid lens resembles that of a drop on a substrate but now consists of two spherical caps: one cap above and one cap below the surface of the liquid pool.

In contrast to spherical drops, the geometry of sessile drops does not exhibit axisymmetry. Despite the intricate geometry, when viewed from the side the problem resembles that of two wedges of fluid, of angle θ , which are gently brought into contact (cf. inset of **Figure 3b**, also for the definition of the bridge height b_0). As for conical drops, such wedges fall in the class of geometrically similar coalescence, for which the drop size has no effect on the initial dynamics of the bridge height. Hence, one obtains the bridge height $b_0 \sim t$ in the viscous regime (Narhe et al. 2008, Hernandez-Sanchez et al. 2012, Hack et al. 2020, Klopp & Eremin 2020, Klopp et al. 2020, Kaneelil et al. 2022, Scheel et al. 2023), while the inertial limit gives $b_0 \sim t^{2/3}$ (Eddi et al. 2013, Sui et al. 2013, Hack et al. 2020), both for sessile drops and for liquid lenses. **Figure 3b** shows experimental data for liquid lenses, crossing over from the viscous to the inertial asymptotes. The data are accurately described by an empirical crossover function (Hack et al. 2020),

$$\frac{b_0}{\ell_v} = f(\xi) = \left[\frac{1}{K_v \xi} + \frac{1}{K_i \xi^{2/3}} \right]^{-1}, \quad \text{with } \xi = \theta^2 t / t_v, \quad 4.$$

with prefactors $K_v = 0.552$ and $K_i = 0.781$, computed from similarity analysis of the thin sheet equations. The crossover only involves intrinsic scales ℓ_v and t_v , reflecting the absence of any external scale for geometrically similar coalescence (in contrast to Equation 2). Importantly, the dependence of $b_0(t)$ on the contact angle θ is different for drops on a substrate and drops on a pool, owing to the different boundary conditions. The scalings in **Tables 1** and **2** are obtained by a refined version of the analysis presented in Section 4, where we do full justice to the three-dimensional aspects of sessile drop coalescence.

2.4. Other Cases

We proceed by briefly discussing coalescence in Hele–Shaw flows and for non-Newtonian fluids.

2.4.1. Drops in Hele–Shaw flow. Hele–Shaw flow consists of a viscous fluid confined between two closely spaced parallel plates (spacing D) (cf. **Figure 1f**). During drop coalescence in a Hele–Shaw cell, there is a short initial regime where the bridge radius $r_0 \ll D$, in which case the confinement does not affect the viscous (linear) bridge scaling. However, quickly one approaches a new regime in which $r_0 \gg D$, so that the flow becomes quasi-two-dimensional (Yokota & Okumura 2011). In this regime, the released capillary energy becomes $E_\gamma \sim \gamma D r_0$. One finds that the shear rate between the plates $\dot{\epsilon} \sim \dot{r}_0 / D$, while the relevant volume $\mathcal{V} \sim r_0 D w$. The power balance then gives $r_0 \sim t^{1/4}$, as observed experimentally.

2.4.2. Non-Newtonian fluids. As illustrated in **Figure 1g**, the Laplace pressure jump is enhanced in polymeric drops due to strong polymer stretching inside the bridge, where deformation rates are large compared to the polymer relaxation time. As a result, coalescing water-based polymeric drops exhibit bridge curvatures that are much larger than those of pure water drops (Bouillant et al. 2022, Dekker et al. 2022). Yet the bridge dynamic $r_0(t)$ was found to be identical to that of pure water drops (Dekker et al. 2022) and bubbles (Oratis et al. 2023): Polymer stretching remains initially confined to a small subregion of the bridge, which, even at a relatively high polymer concentration, makes the influence of polymer stress on the flow too weak to alter the inertial scaling $r_0(t) \sim t^{1/2}$. A polymer-induced slowing down is observed only at slightly later times, with a smaller effective exponent reported for a variety of polymer solutions (Varma et al. 2020). For sessile drops at high concentrations (beyond the dilute regime), such slowing down was observed already for early times (Varma et al. 2021, 2022; Dekker et al. 2022). Other studies involving complex fluids considered how yield stress leads to arrested drop merging (Kern et al. 2022), the effect of shear thinning on the tip structure for bubble coalescence (Kamat et al. 2020), and the coalescence of thin liquid crystal domains (Delabre & Cazabat 2010, Klopp et al. 2024). Shear-thinning sessile drops (Chen et al. 2022) are discussed below.

2.5. Different Transport Mechanisms: A General Scaling Law for Coalescence

n_f : flow index of a power-law fluid (Newtonian, $n_f = 1$; shear thinning, $n_f < 1$)

Early on, Herring (1950) had proposed a unifying framework to understand sintering by various mechanisms for (noninertial) material transport, depending on the material and the temperature. For example, at lower temperatures the bulk material becomes solid, and atoms can no longer move in it. Instead, transport is dominated by loosely bound atoms moving around the surface, driven by surface tension (cf. **Figure 1b**). As a result, the timescale and coalescence exponents are very different from those for viscous flow. Without going into the detailed physics of various possible transport mechanisms, the coalescence dynamics can be deduced from dimensional analysis. For example, in the case of viscous flow, transport is driven by surface tension γ and damped by viscosity η , thus involving a characteristic velocity γ/η and a timescale $\tau_v = R\eta/\gamma$. Another example, in mean curvature flow (covered below), is the normal velocity $\sim A\kappa$, where κ is the mean curvature of the interface; such flows thus involve a transport coefficient $[A] = \text{m}^2/\text{s}$, and the associated timescale becomes $\tau = R^2/A$. Generalizing to different modes of (overdamped) transport, the dynamics involves a transport coefficient $[A] = \text{m}^n/\text{s}$, which naturally gives a timescale $\tau_n = R^n/A$. Power-law fluids driven by surface tension also fall in this class, with $n = 1/n_f$.

Applied to coalescence, scaling laws for the initial stages are of the form

$$\frac{r_0}{R} \sim \left(\frac{t}{\tau_n}\right)^\alpha, \quad \text{with} \quad \tau_n = \frac{R^n}{A}. \quad 5.$$

To find α , we assume the filling of the narrow gap between two spheres is controlled by the single length scale $w = r_0^2/R$ (Herring 1950) (cf. **Figure 4a**). Appealing to the asymptotic equivalence between two- and three-dimensional coalescence, the volume flux of material j , which per unit length of the meniscus has dimensions $[j] = \text{m}/\text{s}$, will be of the form $j \sim Aw^{1-n}$. The gap between the spheres has a (two-dimensional) volume $V \sim r_0w \sim r_0^3/R$, which is thus filled according to $\dot{V} \sim jw \sim Aw^{2-n}$. Solving for $r_0(t)$, one finds the exponent

$$\alpha = \frac{1}{2n-1}. \quad 6.$$

This new scaling law reproduces the usually accepted exponents for coalescence (Kuczynski 1949, Kingery 1960, Eggers et al. 1999). Note that in the viscous case $n = 1$ the coalescence exponent

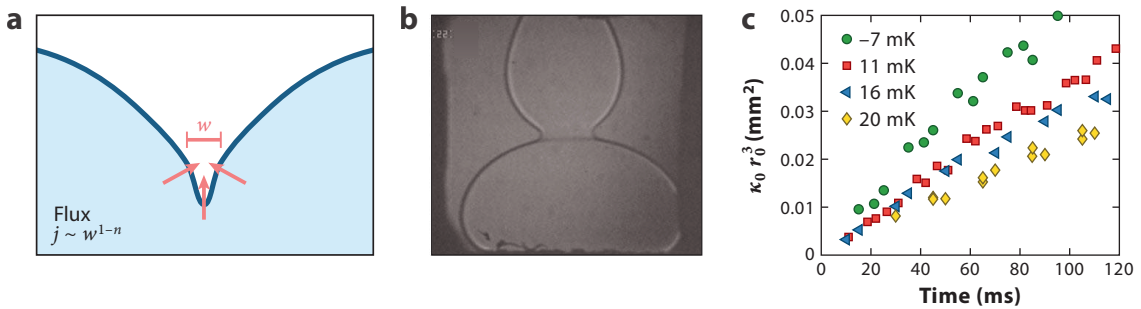


Figure 4

Coalescence beyond viscous transport. (a) The gap of width $w = r_0^2/R$ between two spheres is filled with matter at flux $j \sim w^{1-n}$. Different kinds of transport mechanisms exhibit a different exponent n . (b,c) Mean curvature flow: The flux is proportional to the curvature, $j \sim 1/w$ ($n = 2$). (b) Snapshot during the merging of two ^3He crystals, which evolves according to mean curvature flow (Ishiguro et al. 2004). (c) Cube r_0^3 of the bridge radius (normalized by the mean curvature κ_0 of the initial drops) versus time for different temperatures above (red, blue, and yellow) and below (green) the minimum of the melting curve. The linear trend implies $r_0 \sim t^{1/3}$, in line with Equation 6 (Ishiguro et al. 2004). Panel b adapted with permission from Ishiguro et al. (2004); copyright 2004 American Physical Society.

$\alpha = 1$ is often reported wrongly as $1/2$, which can be traced back to the incorrect argument of Frenkel (1945), alluded to in Section 2.1.

2.5.1. Mean curvature flow ($n = 2$). Mean curvature flow can be realized by the surface of He^3 crystals close to $T_{\min} = 0.32$ K, where the latent heat vanishes and melting and freezing are controlled by small differences in chemical potential (Maris 2003, Ishiguro et al. 2004). As a result, the normal velocity is proportional to the mean curvature. **Figure 4b,c** provides an example of the merging of ^3He crystals (Ishiguro et al. 2004), which follows $r_0 \sim t^{1/3}$, in line with Equation 6 for $n = 2$. The prefactor can be determined analytically from a detailed calculation of the meniscus shape (Maris 2003).

2.5.2. Sintering by volumetric ($n = 3$) or surface ($n = 4$) diffusion. The sintering of metal spheres can be driven by the volumetric diffusion of atoms across the bulk or by the diffusion of atoms along the surface (Kuczynski 1949, Mullins 1959, Eggers 1998). The former involves a transport coefficient with $n = 3$, while the latter has $n = 4$. According to Equation 6, this gives $r_0 \sim t^{1/5}$ and $r_0 \sim t^{1/7}$, respectively, both of which have been observed experimentally (Kuczynski 1949). A closer analysis of merging by surface diffusion, however, reveals that a more subtle argument is needed to derive the growth law (Eggers 1998). The underlying dynamical equation gives rise to surface oscillations: The two sides of the gap between the spheres touch to enclose a void, at which point the dynamics of r_0 restarts. The mechanism of void formation has been used to produce empty structures in silicon (Mizushima et al. 2000).

2.5.3. Other initial conditions. For geometrically similar initial conditions (merging cones) the coalescence dynamics cannot depend on R , which readily implies $\alpha = 1/n$, as is also observed for the blunting of conical tips (Ishiguro et al. 2007, Lamstaes & Eggers 2013). Sessile drop coalescence of power-law fluids is indeed reported to give $\alpha = 1/n = n_f$ (Chen et al. 2022). Another curious case is encountered for the merging of viscous blisters confined between a solid and an elastic sheet; the ratio of the bending modulus and viscosity leads to transport with $n = 3$ (Sæter et al. 2024). Unlike cones or spheres, the initial gap between the blisters is very wide and the dynamics is not governed by a single scale; the growth of the bridge between the blisters is not algebraic but exponential (Sæter et al. 2024).

3. SPHERICAL DROPS

By far the most detailed studies of coalescence have been devoted to the idealized situation of two spherical drops of Newtonian fluid, starting to coalesce at a point of negligible size. Here, the dynamics associated with the approach and reconnection stages is often neglected (see the sidebar titled Practical Challenges, First Contact, and Microscopic Effects). The dynamics is controlled by Oh as a single parameter. We consider the limits of vanishing inertia $\text{Oh} = \infty$ and of inviscid flow $\text{Oh} = 0$ and assess the effect of an outer fluid.

3.1. Very Viscous Drops, $\text{Oh} = \infty$

Let us assume that the shape of the meniscus is described by a similarity solution (Paulsen 2013, Eggers & Fontelos 2015) whose height is set by r_0 and whose width is set by the width $w = r_0^2/R$ of the spacing between two spheres at that scale:

$$r = r_0 \bar{R}(\xi), \quad \text{with} \quad \xi = \frac{zR}{r_0^2}. \quad 7.$$

Here $\bar{R}(\xi)$ is a similarity function to be determined below, which depends on the details of the viscous flow. To make Equation 7 consistent with the shape $r \approx \sqrt{2Rz}$ of two spherical drops that,

PRACTICAL CHALLENGES, FIRST CONTACT, AND MICROSCOPIC EFFECTS

Optical imaging of the initial stages of coalescence is challenging due to the cusp-like gap into which the experimentalist must search for the first signs that merging has occurred. Furthermore, even when electrical methods are used to signify contact (e.g., Thoroddsen et al. 2005a, Paulsen et al. 2011), the mechanism by which contact is established, and thus the initial shapes of the two drops, is unclear.

Throughout the literature, it has been speculated that the intervening air could provide a lubricating cushion that can deform the drops and even prevent contact at the center. To analyze this effect, experiments by Paulsen (2013) vary U over seven orders of magnitude, going as low as 17 nm/s, and show that for approach speeds $< 3 \times 10^{-4}$ m/s, the crossover between viscous and inertial regimes remains unchanged. Recent simulations based on the framework of Sprittles (2024) that includes both gas kinetic effects and van der Waals (vdW) forces between the approaching interfaces support this result (see Deblais et al. 2024). In particular, simulations show a vdW-driven jump to contact that initiates merging of millimeter-sized drops at a distance d_{\min} of tens of nanometers, in agreement with experiment (Chireux et al. 2018). The much larger value of $d_{\min} \sim 160$ nm suggested by Paulsen (2013) is likely due to the strong electric field used there. Clearly, the relation between the approach stage and subsequent coalescence is worthy of further experimental and theoretical analysis; the dynamics of the jump to contact has been investigated theoretically in more detail by Beaty & Lister (2022, 2023).

On top of these effects, one has thermal fluctuations that for typical fluids drive nanoscale interfacial waves that deform the spherical shape of the drops. For larger drops these can act as initial perturbations that initiate the jump-to-contact instability, while for smaller nanodrops they can drive off-center contacts (see Perumanath et al. 2019), introducing stochasticity into the coalescence process.

away from the bridge region, have not yet been deformed, we have to require that $\bar{R} \approx \sqrt{2\xi}$ for large ξ . Even without knowing \bar{R} explicitly, we can conclude that the inverse curvature at the tip, and therefore its smallest length scale Δ , is $r_{zz}^{-1} = r_0^3/(R^2\bar{R}'') \sim r_0^3/R^2$ (Eggers et al. 1999).

To find the time dependence of r_0 (Eggers et al. 1999), one can argue that the flow is driven by surface tension forces, which are concentrated in the highly curved neck region, which forms an azimuthal ring of radius r_0 and produces a force of strength $2\gamma\mathbf{e}_r$ per unit length. On a scale smaller than r_0 , the curvature of the ring can be neglected, and the motion is equivalent to the two-dimensional dynamics of two merging cylinders, driven by two opposite point forces of strength 2γ . This confirms that the leading order asymptotics of two- and three-dimensional coalescence are equivalent, as has been confirmed by numerical simulation (Sprittles & Shikhmurzaev 2014b).

The forcing is opposed by viscous forces, which at a distance r_0 from a two-dimensional point force $F = 2\gamma$ [known as a Stokeslet (Pozrikidis 1992)] produce a velocity $F \ln r_0/(4\pi\eta)$. The forcing is spread out over the local scale $\Delta \sim r_0^3/R^2$ of the tip and cut off over the scale r_0 of the ring, with the opposite side pulling in the opposite direction. This produces a radial velocity of the meniscus $\dot{r}_0 \approx v_\eta/(2\pi) \ln(r_0/\Delta)$, where $v_\eta = \gamma/\eta$ is the capillary velocity. Integrating this velocity, one finds to logarithmically leading order

$$\dot{r}_0 \approx (v_\eta/\pi) \ln(R/r_0), \quad r_0(t) \approx -\frac{v_\eta t}{\pi} \ln(v_\eta t/R). \quad 8.$$

Given the asymptotic equivalence (for early times) of two- and three-dimensional coalescence, an alternative approach is to analyze the exact solution (Hopper 1990, Richardson 1992) of two merging cylinders in Stokes flow. Hopper (1990) found a complex mapping between the cylinders' cross section and the unit disk in terms of a rational function with time-dependent coefficients, describing the entire evolution from reconnection to a single merged circle. Analysis of this mapping yields the minimum radius $r_0/R = \sqrt{2}(1 - a^2)/\sqrt{1 + a^4}$, where the parameter a is shown to

$v_\eta = \gamma/\eta$: capillary velocity, obtained from the balance of surface tension and viscosity

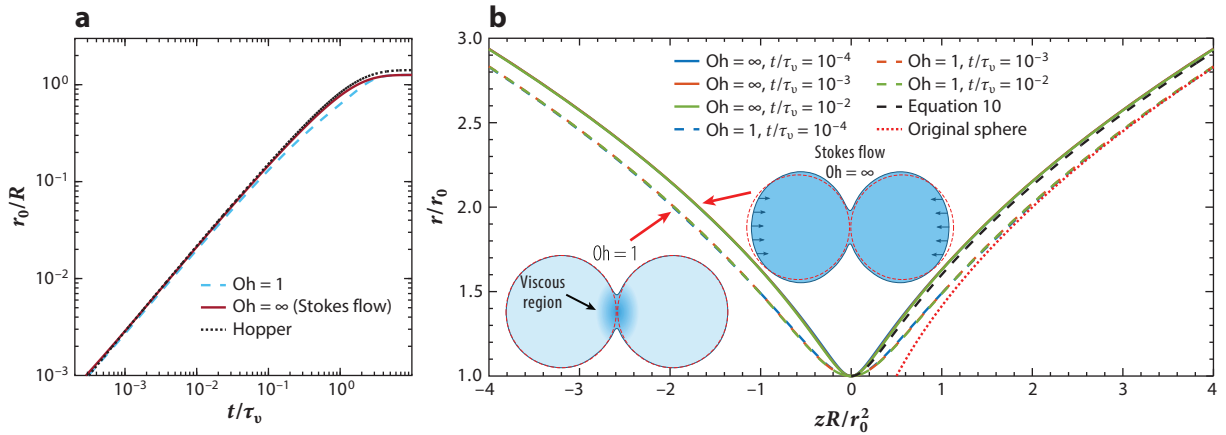


Figure 5

(a) Bridge radius $r_0(t)$ for three-dimensional spherical drop coalescence at $Oh = 1$ and $Oh = \infty$ at early times, compared to Equation 9 (Hopper 1990). (b) Without inertia (Stokes flow) the drop profile near the meniscus collapses for early times onto the similarity solution in Equation 10 (black dashed line). For $Oh = 1$ and early times, collapse is on a different similarity solution, which asymptotes to spheres still at their original position (red dotted line). Figure replotted from simulation data presented by Sprittles & Shikhmurzaev (2014b).

vary with time as

$$\frac{t}{\tau_v} = \frac{\pi}{\sqrt{2}} \int_a^1 \frac{dp}{p\sqrt{1+p^2}K(p)}, \quad 9.$$

and where $K(p)$ is the complete elliptic integral of the first kind (Gradshteyn & Ryzhik 2014). This result matches with Equation 8 at early times, to logarithmically leading order, and agrees very well with numerical simulations of merging spheres and cylinders in the Stokes limit in the absence of an outer atmosphere (Sprittles & Shikhmurzaev 2014b), as is shown in **Figure 5a**. Expanding the entire mapping for $a \approx 1$, one finds the similarity profile corresponding to the similarity solution in Equation 7 to be (Paulsen 2013)

$$\tilde{R}(\xi) = \sqrt{\frac{1}{2} + \sqrt{4\xi^2 + \frac{1}{4}}}, \quad 10.$$

consistent with $\tilde{R} \approx \sqrt{2\xi}$ for large arguments (see also Howison et al. 1997 and Gillow 1998 for a derivation using the slenderness of the cusp). Remarkably, Equation 10 is identical to the similarity solutions describing Moore's instability of vortex sheets (de la Hoz et al. 2008, Eggers & Fontelos 2015) and other nonlocal transport equations (Eggers & Fontelos 2019).

Initial experimental and numerical results for $r_0(t)$ led Paulsen et al. (2012) to hypothesize the existence of a new inertially limited viscous (ILV) regime, in which inertia would intervene to make $r_0(t)$ linear at early times, regardless of the drop viscosity. Theoretically, this was motivated by the fact that inertialess coalescence (i.e., $Oh = \infty$) described by Hopper's (1990) solution drives a uniform translation of both drops by a distance $r_0^2/(4R) = w/4$. This effect is illustrated in **Figure 5b**, showing a horizontal shift of the similarity solution (Equation 10), relative to the original drop position. Estimating drop inertia at finite Oh , it follows that at early times surface tension is not sufficiently strong to move an entire drop by a distance $w/4$; thus, outside the viscous bridge region, the drop remains at its original position.

However, as seen in **Figure 5a**, in reality r_0 remains virtually unaffected by drop translation at early times, in agreement with all recent numerical data (Sprittles & Shikhmurzaev 2014b,

Anthony et al. 2023); as a result, r_0 agrees with Hopper's solution, which includes logarithmic corrections (Eggers et al. 1999). In other words, the arguments leading to Equation 8 still hold at early times, even at finite Oh: The bridge region remains purely viscous, and there is no ILV regime for $r_0(t)$. However, a closer inspection of the self-similar meniscus region (**Figure 5b**) shows that a finite Oh value (Oh = 1) does change the similarity function $\tilde{R}(\xi)$ (cf. Equation 10). Numerical solutions for Oh = 1 collapse onto this new similarity profile, which now has to fit onto the unshifted drop and thus differs from its Oh = ∞ version in Equation 10.

3.2. Inviscid Drops, Oh = 0

In the viscously dominated case, the dynamics was taking place over a wide range of scales, between r_0^3/R^2 and r_0 . In the inviscid case, by contrast, the dynamics is local; the only available length scale is the neck width $w = r_0^2/R$. Invoking this length in the energy balance gives the inviscid scaling (see Section 2.2),

$$r_0 = C_i \left(\frac{\gamma R}{\rho} \right)^{1/4} t^{1/2}. \quad 11.$$

This result has been obtained by a variety of essentially equivalent arguments (Eggers et al. 1999, Duchemin et al. 2003, Biance et al. 2004) and has been proven robust in many experiments (Wu et al. 2004, Case & Nagel 2008, Paulsen 2013, Chireux et al. 2021) and simulations (Sprittles & Shikhmurzaev 2014a,b). The constant is found to be close to $C_i \approx 1.5$ in experiment (see **Figure 2**) and simulations (Sprittles & Shikhmurzaev 2014a), with a slightly higher value of $C_i \approx 1.62$ given by Paulsen (2013). Once again, the local dynamics is controlled by the large curvature near the tip, much larger than the azimuthal curvature of the liquid bridge connecting the drops (Eggers et al. 1999). Thus coalescence in two and three dimensions leads to the same bridge dynamics in the limit of small r_0 . A first correction to Equation 11 can be derived by including the azimuthal curvature (Sprittles & Shikhmurzaev 2014a, Xia et al. 2019), which significantly improves the agreement with numerical simulations for $r_0/R \gtrsim 0.1$.

To analytically determine the prefactor C_i of the inviscid scaling, one might be tempted to resort to a similarity analysis as for the viscous case. Experimental profiles indeed exhibit a reasonable collapse (Dekker et al. 2022) when scaling radial and axial scales with r_0 and w , respectively, in line with Equation 7. However, such a local similarity description only applies in an approximate sense. Duchemin et al. (2003) theoretically analyzed inviscid coalescence assuming potential flow and ignoring the effect of the outer atmosphere. However, the bridge dynamics led to capillary waves fed by a growing bulbous end, and eventually reconnection (Duchemin et al. 2003, Billingham & King 2005), after a time $\tau_0 \sqrt{\rho w^3/\gamma}$, the meniscus having traveled a distance $\Delta_0 w$; the dimensionless constants $\tau_0 = 10$ and $\Delta_0 = 7.6$ were determined numerically. Averaging over many reconnection events (Eggers 1998), one obtains $C_i = \sqrt{2\Delta_0/\tau_0} \approx \sqrt{20/7.6} \approx 1.62$. At the discrete reconnection events, the profile is described approximately by Equation 7; however, this is not an example of discrete self-similarity (Eggers & Fontelos 2015), since reconnection times do not scale geometrically. The reconnections can be suppressed by including the outer fluid into the description (Sprittles & Shikhmurzaev 2014b). As is discussed below, the presence of an outer fluid also introduces a new length scale in the problem, breaking the similarity form in Equation 7.

3.3. An Outer Fluid

Unavoidably, physical systems involve the presence of an outer fluid, most often a gas atmosphere. This introduces the density ratio ρ/ρ_o and most importantly the viscosity ratio $\lambda = \eta/\eta_o$ between

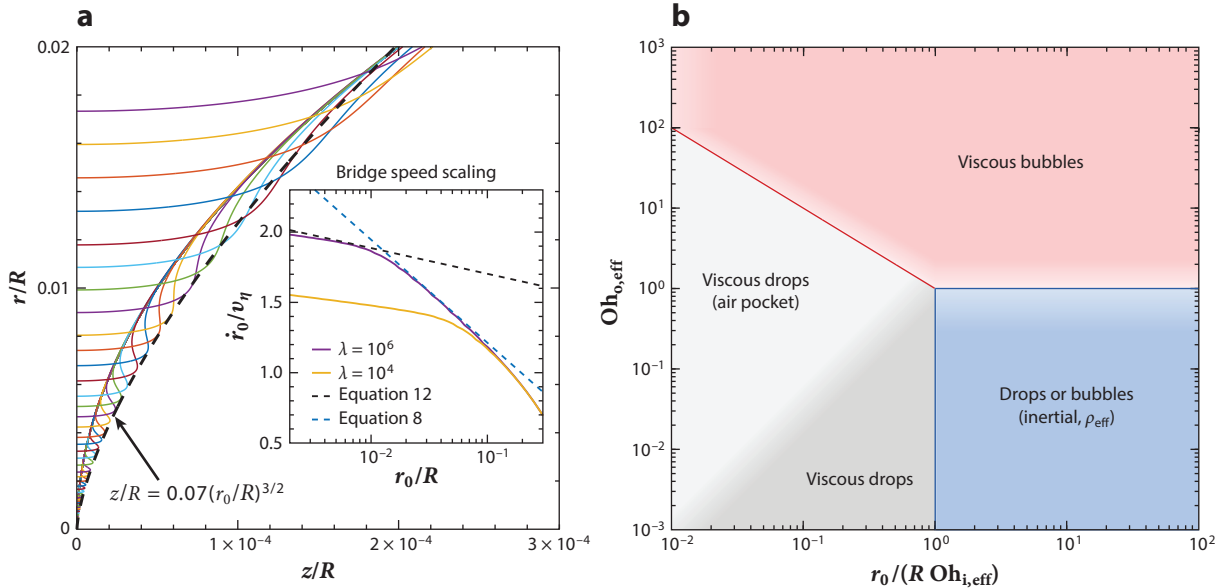


Figure 6

(a) Numerical simulation of spherical coalescence for Stokes flow, including the effect of the outer fluid ($Oh = \infty$, viscosity ratio $\lambda = 10^4$). We observe the appearance and growth of an air pocket that is consistent with all outer fluid accumulating at the meniscus; the inset shows the bridge velocity for $\lambda = 10^4$ and 10^6 according to Equation 12 (including the effect of the outer fluid) and Equation 8 (neglecting the outer fluid). This is replotted from simulation data presented by Sprittles & Shikmurzaev (2014b). (b) Phase map for spherical coalescence in an outer fluid. We defined an effective Ohnesorge number for the inner and outer fluids, using the effective density $\rho_{\text{eff}} = \rho + \rho_o$; hence, $Oh_{i/o,\text{eff}} = \eta_{i/o}/\sqrt{\gamma R \rho_{\text{eff}}}$. The transition in the gray zone is not universal (here sketched for $Oh_{i,\text{eff}} = 1$). Panel b modeled after concepts presented in Paulsen et al. (2014).

the inner and outer fluids as additional parameters. Even the smallest external viscosity will lead to a significant change in behavior (Eggers et al. 1999), as the external fluid is trapped inside a very narrow channel between the two drops, from which it cannot escape. As a result, the outer fluid accumulates inside the meniscus region, forming a toroidal bubble (see **Figure 6a**), as has been observed experimentally for drop coalescence in oil (Aryafar & Kavehpour 2008), in air (Deblais et al. 2024), and in numerical simulations (Sprittles & Shikmurzaev 2014b). The volume of the toroidal bubble follows from integrating over the width of the gap $z = r^2/R$ from 0 to r_0 , which gives $\mathcal{V}_b = \pi r_0^4/(2R)$. This leads to a toroidal bubble of radius $r_b \sim r_0^{3/2}/R^{1/2}$, as confirmed in **Figure 6a**.

3.3.1. Viscous drops. For drops of high viscosity (large Oh) without outer fluid, the dynamics involves the meniscus curvature $\Delta \sim r_0^3/R^2$ as the smallest scale. Due to the presence of the toroidal bubble, the smallest scale is replaced by the bubble size $r_b \sim r_0^{3/2}/R^{1/2}$, changing the dynamics to (Eggers et al. 1999)

$$\dot{r}_0 \approx \frac{v_\eta}{2\pi} \ln(r_0/r_b) \approx \frac{v_\eta}{4\pi} \ln(R/r_0), \quad r_0(t) \approx -\frac{v_\eta t}{4\pi} \ln(v_\eta t/R). \quad 12.$$

Compared to Equation 8, this induces a slower dynamics, by a factor of 4, compared to viscous coalescence without an outer fluid. The scaling in Equation 12 is confirmed numerically (**Figure 6a**, inset), which shows the speed of retraction \dot{r}_0 as a function of r_0 . Even for a very large viscosity ratio λ (small external velocity), Equation 12 is observed at early times. The dynamics crosses over to Equation 8 at the later stages, during which the outer fluid escapes and the toroidal

bubble disappears. The range of r_0 values for which a toroidal bubble is sustained has been estimated as $r_0/R \lesssim \lambda^{-2/3}$ by comparing the pressure inside the drop to the lubrication pressure due to the emptying of the bubble inside the drop (Eggers et al. 1999). An analysis of numerical data by Sprittles & Shikhmurzaev (2014b) indicates $r_0/R \lesssim \lambda^{-1/3}$; the origin of this discrepancy is not known.

The above pertains to small external viscosity ($\lambda \gg 1$). The regime where the outer fluid has comparable or large viscosity ($\lambda \lesssim 1$) has been investigated by Paulsen et al. (2014), for which the toroidal bubble gives way to a smoothened profile (Eggers et al. 1999, Munro et al. 2015). Using the results in **Table 1** for the idealized cases $\lambda = \infty$ (drops) and $\lambda = 0$ (bubbles), we estimate the relative importance of dissipation in the outer/inner fluid, $P_o/P_i \sim \lambda^{-1} r_0/R$. Hence, crossover between dominance of viscous effects of the inner fluid and dominance of the outer fluid takes place at $r_0/R \sim \lambda = \eta/\eta_o$ (Paulsen et al. 2014).

3.3.2. Inviscid drops. Turning to the case of inertially dominated drops (small Oh), for small r_0/R the lubrication pressure in the air pocket strongly inhibits the reconnection of the two sides of the drops. In addition, even if the drop viscosity is small, the resisting factor is now the fluid inertia, which has to be accelerated by the stress exerted by the gas. One can theoretically exploit the presence of the toroidal bubble, as the configuration is identical to the film retraction encountered during inviscid bubble coalescence described in Section 2.2.4, the only difference being the effective mass $\alpha \rho \mathcal{V}_b$ in the exterior of the toroidal bubble; α is an added mass coefficient (Batchelor 1967), which is unity in the case of a circular bubble in two dimensions. The modified result from Keller (1983) then reads $C_i = (32/(3\alpha))^{1/4} \approx 1.8$, with the inertial timescale τ_i based on the density of the drop. In the two-fluid case, the total mass set into motion reads $\rho_{\text{eff}} \mathcal{V}$, with effective density $\rho_{\text{eff}} \approx \rho + \rho_o$. We therefore propose $r_0/R \sim (t/\tau_{i,\text{eff}})^{1/2}$ as a good approximation for inviscid two-fluid coalescence, with an effective inertial time $\tau_{i,\text{eff}}$ based on ρ_{eff} .

3.3.3. Regime map. The relative roles of inner/outer fluids are summarized in a regime map (**Figure 6b**). Since the effect of inertia is captured by ρ_{eff} , we define effective Ohnesorge numbers for the inner/outer fluid as $\text{Oh}_{i/o,\text{eff}} = \eta_{i/o}/\sqrt{\gamma R \rho_{\text{eff}}}$. The vertical axis depends on material properties, while the horizontal axis involves the size of the bridge r_0 , which grows in time. Irrespective of $\text{Oh}_{o,\text{eff}}$, the asymptotics for $r_0 \rightarrow 0$ is always viscous with $r_0 \sim t \ln t$. Initially, the outer fluid collects in an air pocket and the dynamics follows Equation 12. At small outer viscosity ($\text{Oh}_{o,\text{eff}} \lesssim 1$), the air escapes over time and the dynamics gives way to the Hopper solution in Equation 8 (**Figure 6a**) before crossing over into the inertial regime with $r_0 \sim t^{1/2}$. At large outer viscosity ($\text{Oh}_{o,\text{eff}} \gtrsim 1$), the outer fluid never escapes the pocket and the inertial regime is not reached. Instead, one crosses directly from Equation 12 to the viscous bubble regime $r_0 \sim t^{1/2}$.

4. SESSILE DROPS

Sessile drops on a solid substrate or floating on another liquid take the shape of spherical caps. On a (super-)hydrophobic surface, the droplet contact angle $\theta > 90^\circ$ and the initial contact occurs at a finite height above the substrate; the initial dynamics of the small liquid bridge is not influenced by the substrate and follows that of spherical drops (Keij et al. 2013), and the released kinetic energy can even lead to droplet jumping (Charles & Mason 1960b, Thoroddsen & Takehara 2000, Boreyko & Chen 2009). Here we are interested in cases with $\theta \leq 90^\circ$, such that the drop coalescence starts at the substrate. The bridge takes the form of a saddle, described by a function $b(x, y, t)$ (**Figure 7**). The bridge height $b_0(t)$ and bridge width $y_0(t)$ are defined, respectively, from the side view and top view perspectives.

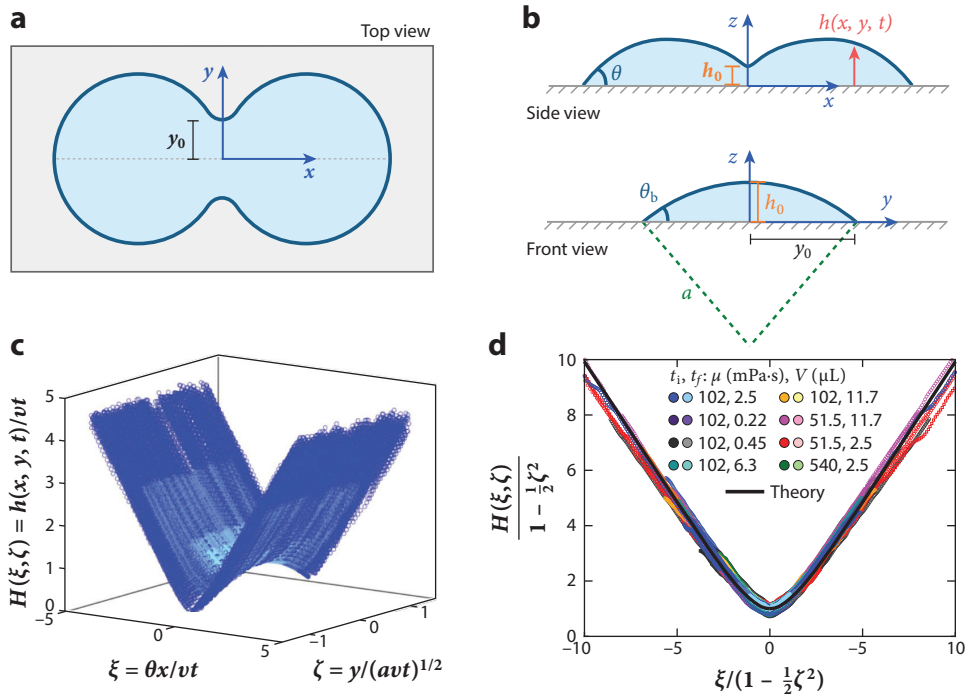


Figure 7

Three-dimensional coalescence of drops on a substrate. (a) Schematic representing the top view defining bridge width y_0 . (b) Schematic representing the side view defining bridge height h_0 and the contact angle θ ; the front view shows the cross section of the liquid bridge with the bridge angle θ_b and bridge radius of curvature a . Lower panels show experimental profiles of the bridge region during the coalescence of viscous silicone oil drops on a glass substrate (Kaneelil et al. 2022). (c) Collapse of bridge profiles according to the similarity form in Equation 14, with constant a . (d) Collapse of data for profiles taken at three different y locations, at multiple times, and multiple volumes V , compared to the theoretical prediction $H^{(1)}$ (solid line) obtained from Equation 15. Panels c and d adapted with permission from Kaneelil et al. (2022); copyright 2022 American Physical Society.

As argued in Section 2.3, the bridge height $h_0(t)$ falls in the class of geometrically similar coalescence, which comes with universal exponents $\alpha = 1$ (viscous) and $\alpha = 2/3$ (inertial). However, the geometric relation between top view and side view coalescence of spherical cap-shaped drops is not universal. Following the classification of singularities proposed by Dallaston et al. (2021), we characterize various cases of sessile drop coalescence as point-like ($y_0 \sim h_0$) or as quasi-one-dimensional ($y_0 \gg h_0$).

4.1. Viscous Drops with Small Contact Angles: $\theta \ll 1$

The most detailed understanding of sessile drop coalescence has been achieved in the limit of viscous drops of small contact angles. Below we discuss this limiting case for drops on a substrate and for liquid lenses.

4.1.1. Viscous drops on a substrate. Figure 7c shows experimental profiles of the three-dimensional shape of the bridge for two highly viscous silicone oil drops merging on a glass substrate (Kaneelil et al. 2022). At $t = 0$, coalescence starts at the plane of symmetry $y = 0$,

according to a linear growth $b(x = 0, y = 0, t) \equiv b_0(t) = vt$. Away from the centerline ($y \neq 0$), the coalescence starts slightly later, at a time $t_0(y)$. Since the bridge is shallow, the cross section in the (yz) -plane is assumed parabolic (**Figure 7c**), so that $vt_0 = y^2/2a$. Here a is the radius of curvature of the bridge, which relates to the bridge width as $y_0 = (2ab_0)^{1/2}$. In experiments for viscous drops, a was found constant in time and set by the global drop size (Kaneelil et al. 2022). Hence, one obtains the bridge width $y_0 \sim t^{1/2}$ (Ristenpart et al. 2006, Narhe et al. 2008), which during the initial stages of coalescence is much larger than the height $b_0 \sim t$. As such, viscous sessile drop coalescence falls in the class of quasi-one-dimensional singularities.

The evolution of $b(x, y, t)$ can be described by two similarity variables: $\xi = x\theta/vt$ in the plane of symmetry and $\zeta = y/\sqrt{avt}$ in the transversal direction. **Figure 7c** shows that this rescaling, combined with b/vt , indeed offers a collapse of experimental profiles taken at different times. With this scaling, a solution of the thin film equation (Eggers & Fontelos 2015),

$$\frac{\partial b}{\partial t} + \frac{\gamma}{3\eta} \nabla \cdot (b^3 \nabla^2 b) = 0, \quad 13.$$

can be written as (Kaneelil et al. 2022)

$$b(x, y, t) = vtH(\xi, \zeta) \equiv vt \left(1 - \frac{1}{2}\zeta^2\right) H^{(1)} \left(\frac{\xi}{1 - \frac{1}{2}\zeta^2}\right). \quad 14.$$

This indeed has the form of a quasi-one-dimensional singularity (Dallaston et al. 2021), where $H^{(1)}$ is a solution of the one-dimensional similarity equation (Hernandez-Sanchez et al. 2012, Kaneelil et al. 2022):

$$H - \xi H' + \frac{1}{A} (H^3 H''')' = 0. \quad 15.$$

The delay time of coalescence in the transverse direction ($\zeta \neq 0$) is accounted for by the factors $1 - \frac{1}{2}\zeta^2$. To mimic the experimental scaling in **Figure 7**, the similarity function was normalized as $H^{(1)}(0) = 1$. This comes at the expense of a constant $A \equiv 3v/(v_\eta\theta^4)$ in Equation 15, which could in fact be scaled out. Its value $A = 0.819$ is determined from the boundary conditions $H'(\infty) = 1$ and $H''(\infty) = 0$ to guarantee matching to the initial drop shape. The solution thus gives the coalescence velocity $v = 0.273v_\eta\theta^4$ (Hernandez-Sanchez et al. 2012), while the shape $H^{(1)}$ in **Figure 7d** is seen to agree very well with experimental data for various cuts at constant y , rescaled according to Equation 14.

4.1.2. Viscous lenses. Coalescence of drops floating on a liquid pool has been studied using top and side view experiments (Burton & Taborek 2007, Hack et al. 2020) and via lattice Boltzmann simulations (Scheel et al. 2023). Another experimental realization consists of viscous lenses confined in very thin freestanding liquid crystal films (Klopp & Eremin 2020, Klopp et al. 2020), which allows for imaging of the droplet profiles by interference (cf. inset **Figure 8a**). In the viscous regime, all studies consistently find that $b_0 \sim y_0 \sim t$. The linear scaling of b_0 in the viscous regime is presented in **Figure 3b**. The fact that y_0 also grows linearly implies that the bridge angle $\theta_b \approx b_0/y_0$ remains approximately constant during coalescence, as shown from the experimental data in **Figure 8a** (Klopp et al. 2020). Viscous lens coalescence therefore corresponds to a two-dimensional singularity of the point-like type (Dallaston et al. 2021), for which the bridge grows with the same scaling in all directions. This is an important difference with respect to the coalescence of a viscous drop on a substrate. Another difference is seen in the growth velocity for the bridge height: $v = 0.55v_\eta\theta^2$ for liquid lenses (Hack et al. 2020) instead of $v = 0.273v_\eta\theta^4$ for drops on a substrate (Hernandez-Sanchez et al. 2012).

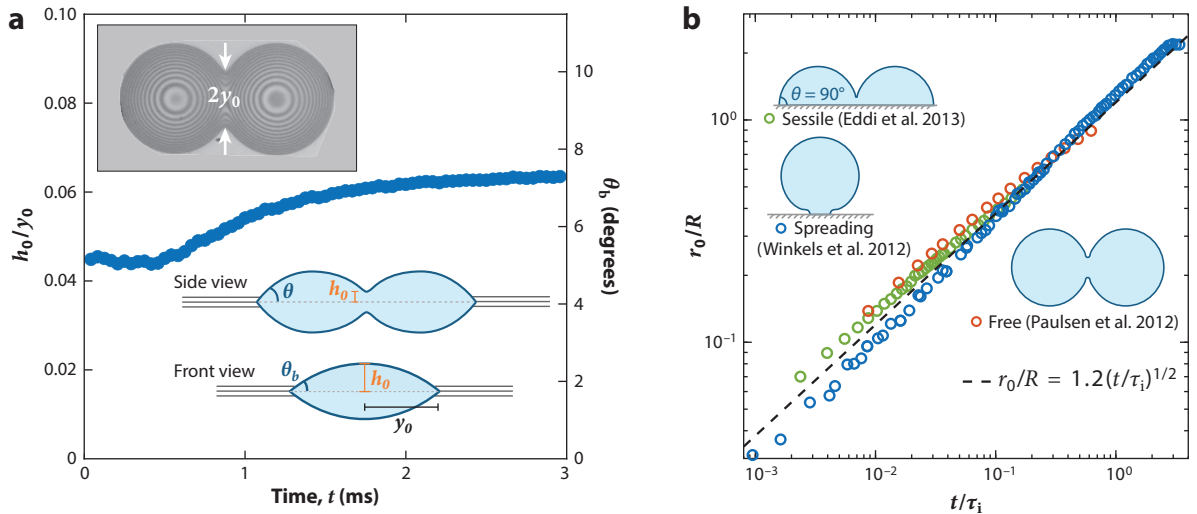


Figure 8

(a) Height-to-width ratio h_0/y_0 during coalescence for viscous lenses, as measured in a freestanding smectic film (Klopp et al. 2020). The ratio remains approximately constant, suggesting a constant bridge angle θ_b . Top left inset provided by Christoph Klopp and Ralf Stannarius. (b) Three cases of water drops with identical dynamics for $r_0(t)$: coalescence of hemispherical sessile drops ($\theta = 90^\circ$, green) (Eddi et al. 2013), spreading drops (blue) (Winkels et al. 2012), and spherical coalescence (red) (Paulsen et al. 2012). The dashed line represents $r_0/R = 1.2(t/\tau_i)^{1/2}$.

4.2. Contact Line Motion

The coalescence of sessile drops gives rise to contact line motion. Below we highlight some salient features associated with this motion and the resulting contact angles.

4.2.1. Top view versus side view. The transverse motion during the coalescence of viscous drops on a solid substrate involves rapidly advancing contact lines. At $x = 0$, according to Equation 14, the contact line position is $y_0(t) \approx (2avt)^{1/2}$ (with constant bridge curvature a): The contact line advances at a speed that is formally diverging for $t \rightarrow 0$. At the same time, the apparent bridge contact angle θ_b , defined in Figure 7c, is $\theta_b \approx \sqrt{2vt/a}$, which goes to zero at initial time $t = 0$. This is a remarkable feature, given that contact lines rapidly advancing over solid surfaces usually lead to an enhancement of the apparent contact angle (compared to the equilibrium angle θ).

We have already seen for viscous drops that the relation between the top view and side view is not universal (constant a on a substrate versus constant θ_b for lenses). The inertial regime probed by water drops on a substrate ($\theta \approx 70^\circ$) shows both h_0 and y_0 to scale with the inertial exponent $2/3$, with $\theta_b \approx \theta$ (Eddi et al. 2013), yet corresponding numerical simulations report an exponent $1/2$ for y_0 (Sui et al. 2013). Likewise, experiments (Burton & Taborek 2007) and numerics (Scheel et al. 2023) for inertial lenses report $y_0 \sim t^{1/2}$ (while we recall $h_0 \sim t^{2/3}$). In general, it is not understood when sessile drop coalescence exhibits $y_0 \sim h_0$ (point-like singularity) or $y_0 \gg h_0$ (quasi-one-dimensional singularity).

4.2.2. Hemispherical drops: $\theta = 90^\circ$. A special case arises when $\theta = 90^\circ$, for which the droplets form perfect hemispheres. Figure 8b shows experimental results for water drops (inertial regime), showing $h_0(t) \sim t^{1/2}$ (Eddi et al. 2013). Within experimental uncertainty, the data are indistinguishable from $r_0(t)$ obtained for spherical coalescence for which no substrate is present. Hence, the

substrate has no measurable effect on the bridge growth. We recall that water drops on a substrate that meet with $\theta < 90^\circ$ exhibit an initial dynamics $h_0 \sim t^{2/3}$. For angles close to (but smaller than) $\theta = 90^\circ$, the $2/3$ scaling is observed only over a very short time, quickly crossing over to the $1/2$ regime (Sui et al. 2013).

4.2.3. The spreading-coalescence analogy. When a droplet is deposited very gently on a substrate, with negligible impact velocity, a very rapid contact line motion ensues (see inset in **Figure 8**). Interestingly, the dynamics of the contact radius for the initial spreading of water drops follows $r_0 \sim t^{1/2}$ (Biance et al. 2004, Carlson et al. 2011, Winkels et al. 2012, Stapelbroek et al. 2014), and an analogy with inertial coalescence was already suggested by Biance et al. (2004). **Figure 8b** directly compares the liquid bridge dynamics $r_0(t)$ for initial spreading and for the coalescence of water drops: The datasets nearly fall on top of one another, the best fits giving prefactors $C_i = 1.5$ (coalescence) and $C_i = 1.2$ (spreading). Once again, the presence of a moving contact line has little effect on the initial dynamics of the bridge, even upon changing the wettability (from $\theta = 0^\circ$ to 115°) or various types of substrate inhomogeneities (Winkels et al. 2012, Stapelbroek et al. 2014). The spreading-coalescence analogy is also observed for water drops with (voltage-induced) conical tips: Both spreading and coalescence exhibit $r_0 \sim t^{2/3}$ (Courbin et al. 2009).

FUTURE ISSUES

1. The hydrodynamics of just two drops colliding at finite speed is quite complicated, and many aspects remain unexplored.
2. Our findings in Section 3.1 suggest the existence of a second similarity solution describing viscous coalescence, but at finite Oh. The mechanism by which inertia comes into play remains to be discovered.
3. The observation or prediction of entrapped toroidal bubbles during the coalescence of low-viscosity drops remains an intriguing possibility. While conventional lubrication in the gas prevents their formation, it is possible that in narrow gaps kinetic effects reduce the apparent viscosity of the gas and conspire with van der Waals forces to entrap a trail of bubbles.
4. How the outer fluid combines with microscopic effects to provide an initial condition for coalescence deserves further attention. How are the approach, reconnection, and coalescence phases related?
5. For the coalescence of sessile drops, the relation between the bridge height and the bridge width is not universal and not understood.
6. What is the effect of contact line motion on coalescence on a substrate? Why does the contact line hardly influence the initial stages of spreading?

DISCLOSURE STATEMENT

The authors are not aware of any affiliations, memberships, funding, or financial holdings that might be perceived as affecting the objectivity of this review.

ACKNOWLEDGMENTS

We thank Christopher Anthony, Osman Basaran, Vincent Bertin, Daniel Bonn, Antoine Deblais, Antonin Eddi, Marco Fontelos, Jens Harting, Paul Kaneelil, Christoph Klopp, John Lister, James

Munro, Alex Oratis, Joseph Paulsen, Etienne Rolley, Thomas Scheel, Ralf Stannarius, and Howard Stone for discussions and/or exchange of data. We are grateful to Alex Oratis for his help with the figures. J.E. was supported by a Wolfson Research Merit Award of the Royal Society. J.E.S. acknowledges funding from the Leverhulme Trust and multiple Engineering and Physical Sciences Research Council grants, most notably EP/W031426/1, EP/S029966/1, EP/P031684/1, and EP/N016602/1. J.H.S. was supported by the Dutch Research Council (NWO) through VICI grant 680-47-632.

LITERATURE CITED

- Aarts DGAL, Lekkerkerker HNW, Guo H, Wegdam GH, Bonn D. 2005. Hydrodynamics of droplet coalescence. *Phys. Rev. Lett.* 95:164503
- Anthony CR, Harris MT, Basaran OA. 2020. Initial regime of drop coalescence. *Phys. Rev. Fluids* 5:033608
- Anthony CR, Kamat PM, Thete SS, Munro JP, Lister JR, et al. 2017. Scaling laws and dynamics of bubble coalescence. *Phys. Rev. Fluids* 2:083601
- Anthony CR, Wee H, Garg V, Thete SS, Kamat PM, et al. 2023. Sharp interface methods for simulation and analysis of free surface flows with singularities: breakup and coalescence. *Annu. Rev. Fluid Mech.* 55:707–47
- Aryafar H, Kavehpour HP. 2008. Hydrodynamic instabilities of viscous coalescing droplets. *Phys. Rev. E* 78:037302
- Ashgriz N, Poo JY. 1990. Coalescence and separation in binary collisions of liquid drops. *J. Fluid Mech.* 221:183–204
- Baroudi L, Kawaji M, Lee T. 2014. Effects of initial conditions on the simulation of inertial coalescence of two drops. *Comput. Math. Appl.* 67:282–89
- Baroudi L, Nagel SR, Lee T. 2016. Comment on viscous coalescence of droplets: a lattice Boltzmann study. *Phys. Fluids* 28:079101
- Bartlett CT, Généro GA, Bird JC. 2015. Coalescence and break-up of nearly inviscid conical droplets. *J. Fluid Mech.* 763:369–85
- Batchelor GK. 1967. *An Introduction to Fluid Dynamics*. Cambridge, UK: Cambridge Univ. Press
- Beaty E, Lister JR. 2022. Nonuniversal self-similarity for jump-to-contact dynamics between viscous drops under van der Waals attraction. *Phys. Rev. Lett.* 129:064501
- Beaty E, Lister JR. 2023. Inertial and viscous dynamics of jump-to-contact between fluid drops under van der Waals attraction. *J. Fluid Mech.* 957:A25
- Biance AL, Clanet C, Quéré D. 2004. First steps of the spreading of a liquid droplet. *Phys. Rev. E* 69:016301
- Billingham J, King AC. 2005. Surface-tension-driven flow outside a slender wedge with an application to the inviscid coalescence of drops. *J. Fluid Mech.* 533:193–221
- Bird JC, Ristenpart WD, Belmonte A, Stone HA. 2009. Critical angle for electrically driven coalescence of two conical droplets. *Phys. Rev. Lett.* 103(16):164502
- Boreyko JB, Chen CH. 2009. Self-propelled dropwise condensate on superhydrophobic surfaces. *Phys. Rev. Lett.* 103(18):184501
- Bouillant A, Dekker PJ, Hack MA, Snoeijer JH. 2022. Rapid viscoelastic spreading. *Phys. Rev. Fluids* 7(12):123604
- Burton JC, Taborek P. 2007. Role of dimensionality and axisymmetry in fluid pinch-off and coalescence. *Phys. Rev. Lett.* 98(22):224502
- Caragine CM, Haley SC, Zidovska A. 2018. Surface fluctuations and coalescence of nucleolar droplets in the human cell nucleus. *Phys. Rev. Lett.* 121:148101
- Carlson A, Do-Quang M, Amberg G. 2011. Dissipation in rapid dynamic wetting. *J. Fluid Mech.* 682:213–40
- Case SC, Nagel SR. 2008. Coalescence in low-viscosity liquids. *Phys. Rev. Lett.* 100:084503
- Chan DYC, Klaseboer E, Manic R. 2011. Film drainage and coalescence between deformable drops and bubbles. *Soft Matter* 7:2235–64
- Charles GE, Mason SG. 1960a. The coalescence of liquid drops with flat liquid/liquid interfaces. *J. Colloid Sci.* 15:236–67

- Charles GE, Mason SG. 1960b. The mechanism of partial coalescence of liquid drops at liquid/liquid interfaces. *J. Colloid Sci.* 15:105–22
- Chen H, Pan X, Nie Q, Ma Q, Fang H, Yin Z. 2022. Probing the coalescence of non-Newtonian droplets on a substrate. *Phys. Fluids* 34(3):032109
- Chesters AK. 1991. The modelling of coalescence processes in fluid-liquid dispersions: a review of current understanding. *Chem. Engin. Res. Des.* 69:259–70
- Chireux V, Protat M, Risso F, Ondarcuhu T, Tordjeman P. 2018. Jump-to-contact instability: the nanoscale mechanism of droplet coalescence in air. *Phys. Rev. Fluids* 3:102001(R)
- Chireux V, Tordjeman P, Risso F. 2021. Bridge expansion after coalescence of two droplets in air: inertial regime. *Phys. Fluids* 33:06112
- Courbin L, Bird JC, Reyssat M, Stone HA. 2009. Dynamics of wetting: from inertial spreading to viscous imbibition. *J. Phys. Condens. Matter* 21(46):464127
- Culick FEC. 1960. Comments on a ruptured soap film. *J. Appl. Phys.* 31:1128–29
- Dallaston MC, Fontelos MA, Herrada MA, Lopez-Herrera JM, Eggers J. 2021. Regular and complex singularities of the generalized thin film equation in two dimensions. *J. Fluid Mech.* 917:A20
- Davis R, Schonberg J, Rallison J. 1989. The lubrication force between two viscous drops. *Phys. Fluids* 1:77–81
- de Gennes P-G, Brochart-Wyart F, Quéré D. 2004. *Capillarity and Wetting Phenomena: Drops, Bubbles, Pearls, Waves*. New York: Springer
- de la Hoz F, Fontelos MA, Vega L. 2008. The effect of surface tension on the Moore singularity of vortex sheet dynamics. *J. Nonlinear Sci.* 18:463–84
- de la Mora JF. 2007. The fluid dynamics of Taylor cones. *Annu Rev. Fluid Mech.* 39:217–43
- Deblais A, Xie K, Lewin-Jones P, Aarts D, Herrada MA, et al. 2024. Early stages of drop coalescence. arXiv:2402.00500 [physics.flu-dyn]
- Dekker PJ, Hack MA, Tewes W, Datt C, Bouillant A, Snoeijer JH. 2022. When elasticity affects drop coalescence. *Phys. Rev. Lett.* 128:028004
- Delabre U, Cazabat AM. 2010. Coalescence driven by line tension in thin nematic films. *Phys. Rev. Lett.* 104(22):227801
- Duchemin L, Eggers J, Josserand C. 2003. Inviscid coalescence of drops. *J. Fluid Mech.* 487:167–78
- Eddi A, Winkels KG, Snoeijer JH. 2013. Influence of droplet geometry on the coalescence of low viscosity drops. *Phys. Rev. Lett.* 111(14):144502
- Eggers J. 1993. Universal pinching of 3D axisymmetric free-surface flow. *Phys. Rev. Lett.* 71:3458–60
- Eggers J. 1997. Nonlinear dynamics and breakup of free-surface flows. *Rev. Mod. Phys.* 69:865–929
- Eggers J. 1998. Coalescence of spheres by surface diffusion. *Phys. Rev. Lett.* 80:2634–37
- Eggers J, Fontelos MA. 2015. *Singularities: Formation, Structure, and Propagation*. Cambridge, UK: Cambridge Univ. Press
- Eggers J, Fontelos MA. 2019. Selection of singular solutions in non-local transport equations. *Nonlinearity* 33:325
- Eggers J, Lister JR, Stone HA. 1999. Coalescence of liquid drops. *J. Fluid Mech.* 401:293–310
- Eggers J, Villermaux E. 2008. Physics of liquid jets. *Rep. Progr. Phys.* 71:036601
- Fezzaa K, Wang Y. 2008. Ultrafast x-ray phase-contrast imaging of the initial coalescence phase of two water droplets. *Phys. Rev. Lett.* 100:104501
- Flenner E, Janosi L, Barz B, Neagu A, Forgacs G, Kosztin I. 2012. Kinetic Monte Carlo and cellular particle dynamics simulations of multicellular systems. *Phys. Rev. E* 85:031907
- Frenkel J. 1945. Viscous flow of crystalline bodies under the action of surface tension. *J. Phys.* 9:385–91
- Gillow K. 1998. *Codimension-two free boundary problems*. PhD Thesis, Univ. Oxford, Oxford, UK
- Gradshteyn IS, Ryzhik IM. 2014. *Table of Integrals Series and Products*. New York: Academic
- Grosser S, Lippoldt J, Oswald L, Merkel M, Sussman DM, et al. 2021. Cell and nucleus shape as an indicator of tissue fluidity in carcinoma. *Phys. Rev. X* 11:011033
- Hack MA, Tewes W, Xie Q, Datt C, Harth K, et al. 2020. Self-similar liquid lens coalescence. *Phys. Rev. Lett.* 124(19):194502
- Hernandez-Sanchez JF, Lubbers LA, Eddi A, Snoeijer JH. 2012. Symmetric and asymmetric coalescence of drops on a substrate. *Phys. Rev. Lett.* 109:104501

- Herring C. 1950. Effect of change of scale on sintering phenomena. *J. Appl. Phys.* 21:301–3
- Hopper RW. 1990. Plane Stokes flow driven by capillarity on a free surface. *J. Fluid Mech.* 213:349–75
- Hopper RW. 1991. Plane Stokes flow driven by capillarity on a free surface. Part 2. Further developments. *J. Fluid Mech.* 230:355–64
- Howison SD, Morgan JD, Ockendon JR. 1997. A class of codimension-two free boundary problems. *SIAM Rev.* 39:221–53
- Ishiguro R, Graner F, Rolley E, Balibar S. 2004. Coalescence of crystalline drops. *Phys. Rev. Lett.* 93:235301
- Ishiguro R, Graner F, Rolley E, Balibar S, Eggers J. 2007. Dripping of a crystal. *Phys. Rev. E* 75:041606
- Kamat PM, Anthony CR, Basaran OA. 2020. Bubble coalescence in low-viscosity power-law fluids. *J. Fluid Mech.* 902:A8
- Kamp J, Villwock J, Kraume M. 2017. Drop coalescence in technical liquid/liquid applications: a review on experimental techniques and modeling approaches. *Rev. Chem. Eng.* 33:1–47
- Kaneelil PR, Pahlavan AA, Xue N, Stone HA. 2022. Three-dimensional self-similarity of coalescing viscous drops in the thin-film regime. *Phys. Rev. Lett.* 129(14):144501
- Kavehpour HP. 2015. Coalescence of drops. *Annu. Rev. Fluid Mech.* 47:245–68
- Keij DL, Winkels KG, Castelijn H, Riepen M, Snoeijer JH. 2013. Bubble formation during the collision of a sessile drop with a meniscus. *Phys. Fluids* 25(8):082005
- Keller JB. 1983. Breaking of liquid films and threads. *Phys. Fluids* 26:3451–53
- Keller JB, Milewski PA, Vanden-Broeck JM. 2000. Merging and wetting driven by surface tension. *Eur. J. Mech. B Fluids* 19(4):491–502
- Kern VR, Sæter T, Carlson A. 2022. Viscoplastic sessile drop coalescence. *Phys. Rev. Fluids* 7(8):L081601
- Kingery WD. 1960. Regelation, surface diffusion, and ice sintering. *J. Appl. Phys.* 31:833–38
- Klopp C, Eremin A. 2020. On droplet coalescence in quasi-two-dimensional fluids. *Langmuir* 36(35):10615–21
- Klopp C, Trittel T, Harth K, Stannarius R. 2024. Coalescence of biphasic droplets embedded in free standing smectic A films. *Soft Matter* 20(5):1036–46
- Klopp C, Trittel T, Stannarius R. 2020. Self similarity of liquid droplet coalescence in a quasi-2D free-standing liquid-crystal film. *Soft Matter* 16(19):4607–14
- Kuczynski GC. 1949. Self-diffusion in sintering of metallic particles. *JOM* 185:169–78
- Lamstaes C, Eggers J. 2013. Blunting of conical tips by surface diffusion. *Phys. Rev. E* 87:062408
- Li J. 2016. Macroscopic model for head-on binary droplet collisions in a gaseous medium. *Phys. Rev. Lett.* 117:214502
- Liao Y, Lucas D. 2010. A literature review on mechanisms and models for the coalescence process of fluid particles. *Chem. Eng. Sci.* 65:2851–64
- Lohse D. 2022. Fundamental fluid dynamics challenges in inkjet printing. *Annu. Rev. Fluid Mech.* 54:349–82
- Maris HJ. 2003. Analysis of the early stage of coalescence of helium drops. *Phys. Rev. E* 67:066309
- Menchaca-Rocha A, Martinez-Davalos A, Nunez R, Popinet S, Zaleski S. 2001. Coalescence of liquid drops by surface tension. *Phys. Rev. E* 63:046309
- Miksis MJ, Vanden-Broeck JM. 1999. Self-similar dynamics of a viscous wedge of fluid. *Phys. Fluids* 11(11):3227–31
- Mizushima I, Sato T, Taniguchi S, Tsunashima Y. 2000. Empty-space-in-silicon technique for fabricating a silicon-on-nothing structure. *Appl. Phys. Lett.* 77:3290–92
- Mullins WW. 1959. Flattening of a nearly plane solid surface due to capillarity. *J. Appl. Phys.* 30:77–83
- Munro JP, Anthony CR, Basaran OA, Lister JR. 2015. Thin-sheet flow between coalescing bubbles. *J. Fluid Mech.* 773:R3
- Narhe RD, Beysens DA, Pomeau Y. 2008. Dynamic drying in the early-stage coalescence of droplets sitting on a plate. *Europhys. Lett.* 81:46002
- Nichols FA, Mullins WW. 1965. Morphological changes of a surface of revolution due to capillarity-induced surface diffusion. *J. Appl. Phys.* 36:1826–35
- Oguz HN, Prosperetti A. 1989. Surface-tension effects in the contact of liquid surfaces. *J. Fluid Mech.* 203:149–71
- Oratis AT, Bertin V, Snoeijer JH. 2023. Coalescence of bubbles in a viscoelastic liquid. *Phys. Rev. Fluids* 8(8):083603

- Paulsen JD. 2013. Approach and coalescence of liquid drops in air. *Phys. Rev. E* 88:063010
- Paulsen JD, Burton JC, Nagel SR. 2011. Viscous to inertial crossover in liquid drop coalescence. *Phys. Rev. Lett.* 106:114501
- Paulsen JD, Burton JC, Nagel SR, Appathurai S, Harris MT, Basaran OA. 2012. The inexorable resistance of inertia determines the initial regime of drop coalescence. *PNAS* 109:6857–61
- Paulsen JD, Carmigniani R, Kannan A, Burton JC, Nagel SR. 2014. Coalescence of bubbles and drops in an outer fluid. *Nat. Commun.* 5:3182
- Peregrine DH, Shoker G, Symon A. 1990. The bifurcation of liquid bridges. *J. Fluid Mech.* 212:25–39
- Perumanath S, Borg MK, Chubynsky MV, Sprittles JE, Reese JM. 2019. Droplet coalescence is initiated by thermal motion. *Phys. Rev. Lett.* 122:104501
- Planchette C, Lorenceau E, Brenn G. 2012. The onset of fragmentation in binary liquid drop collisions. *J. Fluid Mech.* 702:5–25
- Pokluda O, Bellehumeur CT, Machopoulos J. 1997. Modification of Frenkel's model for sintering. *AIChE J.* 43:3253–56
- Popinet S. 2018. Numerical models of surface tension. *Annu. Rev. Fluid Mech.* 50:49–75
- Pozrikidis C. 1992. *Boundary Integral and Singularity Methods for Linearized Flow*. Cambridge, UK: Cambridge Univ. Press
- Quinn DB, Feng J, Stone HA. 2013. Analytical model for the deformation of a fluid–fluid interface beneath an AFM probe. *Langmuir* 29:1427–34
- Rahaman MN. 2010. Kinetics and mechanisms of densification. In *Sintering of Advanced Materials*, ed. ZZ Fang, pp. 33–64. Cambridge, UK: Woodhead
- Reynolds O. 1900 (1881). On the floating of drops on the surface of water depending only on the purity of the surface. In *Papers on Mechanical and Physical Subjects*, Vol. 1, pp. 413–14. Cambridge, UK: Cambridge Univ. Press
- Richardson S. 1992. Two-dimensional slow viscous flows with time-dependent free boundaries driven by surface tension. *Eur. J. Appl. Math.* 3:193–207
- Ristenpart WD, McCalla PM, Roy RV, Stone HA. 2006. Coalescence of spreading droplets on a wettable substrate. *Phys. Rev. Lett.* 97:064501
- Ryu S, Zhang H, Anuta UJ. 2023. A review on the coalescence of confined drops with a focus on scaling laws for the growth of the liquid bridge. *Micromachines* 14:2046
- Sæter T, Pedersen C, Snoeijer JH, Salez T, Carlson A. 2024. Coalescence of elastic blisters filled with a viscous fluid. *Phys. Rev. Lett.* 132(7):074001
- Scheel T, Xie Q, Sega M, Harting J. 2023. Viscous to inertial coalescence of liquid lenses: a lattice Boltzmann investigation. *Phys. Rev. Fluids* 8(7):074201
- Sprittles JE. 2024. Gas microfilms in droplet dynamics: When do drops bounce? *Annu. Rev. Fluid Mech.* 56:91–118
- Sprittles JE, Shikhmurzaev YD. 2012. Coalescence of liquid drops: different models versus experiment. *Phys. Fluids* 24:122105
- Sprittles JE, Shikhmurzaev YD. 2014a. Dynamics of liquid drops coalescing in the inertial regime. *Phys. Rev. E* 89:063008
- Sprittles JE, Shikhmurzaev YD. 2014b. A parametric study of the coalescence of liquid drops in a viscous gas. *J. Fluid Mech.* 753:279–306
- Stapelbroek BBJ, Jansen HP, Kooij ES, Snoeijer JH, Eddi A. 2014. Universal spreading of water drops on complex surfaces. *Soft Matter* 10(15):2641–48
- Sui Y, Maglio M, Spelt PDM, Legendre D, Ding H. 2013. Inertial coalescence of droplets on a partially wetting substrate. *Phys. Fluids* 25(10):101701
- Taylor GI. 1959. The dynamics of thin sheets of fluid. III. Disintegration of fluid sheets. *Proc. R. Soc. Lond.* 253:313–21
- Thoroddsen S, Takehara K, Etoh T. 2005a. The coalescence speed of a pendent and a sessile drop. *J. Fluid Mech.* 527:85–114
- Thoroddsen ST, Etoh EG, Takeara K. 2008. High-speed imaging of drops and bubbles. *Annu. Rev. Fluid Mech.* 40:257–85

- Thoroddsen ST, Takehara K. 2000. The coalescence cascade of a drop. *Phys. Fluids* 12(6):1265–67
- Thoroddsen ST, Takehara K, Etoh TG. 2005b. The coalescence speed of a pendent and a sessile drop. *J. Fluid Mech.* 527:85–114
- Tryggvason G, Scardovelli R, Zaleski S. 2011. *Direct Numerical Simulations of Gas–Liquid Multiphase Flows*. Cambridge, UK: Cambridge Univ. Press
- Varma SC, Dasgupta D, Kumar A. 2022. Elasticity can affect droplet coalescence. *Phys. Fluids* 34(9):093112
- Varma SC, Saha A, Kumar A. 2021. Coalescence of polymeric sessile drops on a partially wettable substrate. *Phys. Fluids* 33(12):123101
- Varma SC, Saha A, Mukherjee S, Bandopadhyay A, Kumar A, Chakraborty S. 2020. Universality in coalescence of polymeric fluids. *Soft Matter* 16(48):10921–27
- Verdier C. 2001. The influence of the viscosity ratio on polymer droplet collision in quiescent blends. *Polymer* 42:6999–7007
- Winkels KG, Weijs JH, Eddi A, Snoeijer JH. 2012. Initial spreading of low-viscosity drops on partially wetting surfaces. *Phys. Rev. E* 85(5):055301
- Wu M, Cubaud T, Ho CH. 2004. Scaling law in liquid drop coalescence driven by surface tension. *Phys. Fluids* 16:L51–54
- Xia X, He C, Zhang P. 2019. Universality in the viscous-to-inertial coalescence of liquid droplets. *PNAS* 116:23467–72
- Yao W, Maris HJ, Pennington P, Seidel GM. 2005. Coalescence of viscous liquid drops. *Phys. Rev. E* 71:016309
- Yokota M, Okumura K. 2011. Dimensional crossover in the coalescence dynamics of viscous drops confined in between two plates. *PNAS* 108:6395–98